Flexible and scalable control of T cell memory by a reversible epigenetic switch

Kathleen Abadie[1*], Elisa C. Clark[1*], Obinna Ukogu[2], Wei Yang[3], Riza M. Daza[3], Kenneth K.H. Ng[1], Jumana Fathima[1], Allan L. Wang[1], Avinash Bhandoola[4], Armita Nourmohammad[2,5,6], Jay Shendure[3,7,8,9,11#], Junyue Cao[3,9,10,#], Hao Yuan Kueh[1,11,#]

[1]Department of Bioengineering, University of Washington, Seattle, WA, USA

[2]Department of Applied Mathematics, University of Washington, Seattle, WA, US

[3]Department of Genome Sciences, University of Washington, Seattle, WA, USA

[4]T-Cell Biology and Development Unit, Laboratory of Genome Integrity, Center for Cancer Research, National Cancer Institute, National Institute of Health, Bethesda, MD, USA

[5]Department of Physics, University of Washington, Seattle, WA, USA

[6] Fred Hutchinson Cancer Research Center, Seattle, USA

[7]Brotman Baty Institute for Precision Medicine, Seattle, WA, USA

[8]Allen Discovery Center for Cell Lineage Tracing, Seattle, WA, USA

[9]Howard Hughes Medical Institute, Seattle, WA, USA

[10]Laboratory of Single-cell Genomics and Population Dynamics, The Rockefeller University, New York, NY, USA

[11]Institute for Stem Cell and Regenerative Medicine, University of Washington, Seattle, WA, USA

[*,#]These authors contributed equally to this manuscript

Abstract

The immune system encodes information about the severity of a pathogenic threat in the quantity and type of memory cell populations formed in response. This encoding emerges from the decisions of lymphocytes to maintain or lose self-renewal and memory potential during a challenge. By tracking responding CD8 T cells at the single-cell and clonal lineage level using time-resolved transcriptomics and quantitative live imaging, we identify a remarkably flexible decision-making strategy, whereby T cells initially choose whether to maintain or lose memory potential early after antigen recognition, but following pathogen clearance may regain memory potential if initially lost. Mechanistically, this flexibility is implemented by a *cis*-epigenetic switch that silences the memory regulator TCF1 in a stochastic and reversible manner in response to stimulatory inputs. Mathematical modeling shows how this strategy allows memory T cell numbers to scale robustly with pathogen virulence and immune response magnitudes. We propose that flexibility and stochasticity in cellular decision making ensures optimal immune responses against diverse threats.

39 **Main**

40 The immune system keeps a memory of prior infections with information about the inducing
41 threat. This memory is encoded by the numbers and types of memory lymphocytes generated
42 upon challenge. The quantity of memory T cells, in particular, scales with the magnitude of a
43 prior infection, such that the memory population is a fixed fraction of the T cell number at the
44 infection peak, across a range of pathogenic challenges[1–3]. This scaling in memory production is
45 robust across T cell clones with different epitope specificities and allows the body to generate
46 memory proportional to the severity of the pathogenic challenge. The regulatory mechanisms
47 that enable this critical feature of adaptive immunity are not well understood.

48

49 The size and characteristics of the memory compartment are determined by the fate decision-
50 making strategies of T cells responding to an acute infection[4]. As naive CD8 T cells respond to
51 antigens, they must decide whether and when to maintain long-term viability and self-renewal
52 potential, and thereby persist to form memory cells as the infection is cleared. One class of
53 models posits that cells make this decision early after antigen encounter, and in a mutually
54 exclusive manner with effector differentiation (Fig. 1A)[5–7]. Under this model, memory cells form
55 directly from naive cells without first passing through an effector phase, but through an early
56 lineage bifurcation that concurrently gives rise to short-lived effector cells. A second class of
57 models posits that cells decide later, only after they have undergone effector differentiation (Fig.
58 1A)[8–10]. In this strategy, cytotoxic effectors that maintain memory potential populate the memory
59 compartment upon infection clearance. However, in contrast with both models, it is also possible
60 that this process is inherently flexible[11], such that T cells have multiple opportunities to commit
61 to the memory state. From a social and cognitive sciences perspective[12,13], flexibility in decision

making allows individuals to adapt and better respond to uncertain and dynamic environments; in the immune system, such flexibility may allow T cells to optimize memory formation for threats whose properties might only manifest as they unfold in time. It is unclear whether there exists such flexibility in T cell memory formation and, if so, what its underlying mechanisms and functional roles are.

In this study, we sought to elucidate the memory decision-making dynamics of CD8 T cells by following the regulation of TCF1 (encoded by *Tcf7*), a transcription factor essential for memory cell generation[14]. *Tcf7* is expressed in naive and memory cells, where it is crucial for maintaining self-renewal, and is silenced during effector differentiation, resulting in loss of memory potential and entry into a short-lived state[5,15]. To follow *Tcf7* regulation and memory decision-making in a controlled environment where cells can be continuously observed and signaling inputs carefully manipulated, we developed an *ex vivo* system to mimic stimulation of T cells by acute challenge. Using this system and complementary testing *in vivo*, we uncover a flexible decision-making strategy: T cells can gain or lose memory potential at multiple junctures after antigen encounter, and do so in a stochastic and reversible manner. Mathematical modeling reveals that this flexible decision-making strategy allows for the number of memory cells to scale linearly with total numbers of expanded T cells at the peak of infection, thereby encoding information about the severity of the prior threat.

A minimal *ex vivo* system for effector and memory differentiation

In our system, naive ($CD44^{-}CD62L^{+}$) CD8 T cells with a knock-in YFP reporter for *Tcf7*[16] are activated with plate-immobilized anti-CD3 and anti-CD28 antibodies and IL-2, together with

85 additional cytokines present during acute infection (IL-12, IL-7, and IL-15[17–19]). These
86 conditions minimize variability in the exposure of individual cells to stimulatory signals,
87 enabling cell-intrinsic lineage control mechanisms to be studied apart from environmental
88 heterogeneity.
89
90 In this system, all cells begin dividing rapidly after 24 hours and upregulate the transmembrane
91 glycoprotein CD44, indicating uniform activation (Fig. 1B). Activated cells downregulate *Tcf7*
92 and the lymph node-homing adhesion molecule CD62L, consistent with effector differentiation.
93 The inflammatory cytokines IL-12 and IFN-β1 enhance *Tcf7*-YFP silencing (Fig. 1C, Fig. S1C-
94 D), consistent with their roles in driving effector differentiation[20,21]. When TCR stimulation
95 (anti-CD3/CD28) and inflammation (IL-12) are removed to mimic pathogen clearance, the cells
96 demonstrate a population-level increase in CD62L and *Tcf7*-YFP while continuing to divide, as
97 previously observed[4]. *Tcf7* and CD62L levels are heterogeneous both during stimulation and
98 after removal, suggestive of an early memory and effector differentiation decision. YFP levels
99 closely matched TCF1 protein levels throughout activation, validating use of the reporter in this
100 system (Fig. S1A-B).
101
102 **Naive cells bifurcate early into effectors and memory precursors**
103 To determine whether the heterogeneity in *Tcf7* and CD62L downregulation reflects early
104 memory and effector programming (Fig. 1), we analyzed *ex vivo* activated cells using the
105 temporally-resolved single-cell transcriptome sequencing method, *sci-fate*[22]. Here, metabolic
106 labeling of newly-synthesized transcripts reveals a cell's current activity state apart from its
107 history[22,23] (Fig. 2A). We subjected cells at days 1, 2, and 4 to 4-thiouridine (4sU) pulse-labeling

108 for 2 hrs, followed by sequencing and analysis as previously described[22]. We obtained old and
109 new transcriptomes for ~17,000 single cells, with a median of 17,574 total and 2,529 new
110 transcripts detected per cell (Fig. S2A). To disentangle effector and memory gene programs from
111 other activation-induced programs, we performed an integrative analysis of our temporally-
112 resolved transcriptome data and existing transcription factor (TF) binding data[24] to identify TF
113 modules, consisting of co-regulated groups of TFs and their cognate target genes (see Methods).
114 This analysis revealed two main TF modules, a cell cycle module and a T cell differentiation
115 module, the latter further separable into submodules that included known regulators of effector
116 and memory differentiation (Fig. 2B; Fig. S2C).
117
118 By visualizing cell states using genes in the T cell differentiation module for Uniform Manifold
119 Approximation and Projection (UMAP) dimensionality reduction, we resolved distinct effector
120 and memory states with coherence between timepoints (Fig. 2C; Fig. S2B, D). Unsupervised
121 clustering and differential gene expression analysis revealed distinct early and late (A vs. B)
122 effector (E1 and E2) and memory precursor (MP) states. E1 and E2 cells exhibited higher
123 expression of the effector-associated genes *Gzmb, Ifng, Tbx21, Zeb2,* and *IL12rb2,* while MP
124 cells had higher expression of the stem- and memory-associated factors *Bach2, Lef1, Tcf7, Sell*,
125 and *Slamf6*, and lower expression of effector-associated genes (Fig. 2D-E; Fig. S2E-F;
126 Supplementary Table 1-2)[25]. These differential gene expression patterns were present at day 2
127 and amplified at day 4.
128
129 Consistent with an early fate bifurcation, RNA velocity vectors calculated using reads from
130 newly synthesized transcripts originate from the undifferentiated state (U), and flow along

131 separate effector and memory branches[26] (Fig. 2F). To gain insight into the dynamics of genes
132 differentially regulated between divergent trajectories, we visualized their expression over
133 pseudotime along each trajectory (Fig. 2G; Supplementary Table 3). This analysis, together with
134 RNA velocity and TF activity analysis (Fig. 2H-I), identified effector and memory regulators
135 with greatest differential regulation along their respective trajectories. *Tbx21, Egr1,* and *Irf4*,
136 among other effector regulatory genes, were specifically active along the E1 trajectory, while a
137 distinct set of effector regulators, including *Eomes, Bhlhe40*, *Stat5a* and *Stat3*, characterize the
138 E2 trajectory. This effector heterogeneity and its potential influence on downstream
139 differentiation will be interesting to investigate in future studies but is not further pursued here.
140 Finally, regulators of T cell stemness and survival, including *Tcf7, Myb, Mxd4* and *Fli1*, were
141 active in the MP trajectory. *Tcf7* was the most significantly differentially expressed gene
142 between trajectories, upregulated early along the MP trajectory and absent in both E1 and E2
143 trajectories. Its expression furthermore coincided with that of target genes identified through TF
144 linkage that promote self-renewal, such as *Ikzf2*, *Sesn3*, *Aff3*, and *Pecam1* (CD31). Thus, *Tcf7* is
145 a critical driver of this early divergent memory trajectory in our system.
146

147 **The early effector and memory decision occurs heterogeneously within clones**

148 The divergence of cells into effector and memory lineages, occurring even under the strong,
149 uniform stimulatory conditions of our *ex vivo* system, is suggestive of a cell-intrinsic regulatory
150 mechanism involving *Tcf7* that generates heterogeneity in fate outcomes. To elucidate the degree
151 to which this decision is heterogeneous within cell lineages amid constant environmental signals,
152 we acquired multi-day time-lapse movies of clonal CD8 T cell lineages during activation with
153 continuous measurement of *Tcf7* reporter levels (Fig. 3). As T cells are difficult to track with live

154 imaging due to their high mobility, tendency to adhere to one another, and rapid proliferation, we
155 optimized adhesion conditions and computational analyses that allow continuous tracking of a
156 fate regulating TF across clonal CD8 T cell lineages (Fig. 3; Fig. S3; see Methods)[27]. Using this
157 method, we tracked a total of 120 clonal lineages over 4 days and an average of 4.4 cell
158 generations.
159
160 Naive cells in these time-lapse movies start small, adhere to the antibody-bound plate, acquire
161 CD69 expression, increase dramatically in size, and divide rapidly after 1-2 days (Fig. S3G;
162 Supplemental movie 1). Strikingly, individual activating T cell clones often gave rise to *Tcf7*
163 high and low subpopulations (Fig. 3A; Fig. S3J; Supplementary Movie 1), indicating that the
164 effector and memory decision is made heterogeneously within clones. Of note, *Tcf7* low and high
165 cells showed similar degrees of attachment to the surface, indicating that these intra-clonal
166 differences are not due to differences in TCR stimulation, but more likely due to cell-intrinsic
167 mechanisms generating heterogeneity in *Tcf7* silencing.
168
169 Differences in *Tcf7*-YFP levels after multiple cell divisions likely stem from earlier *Tcf7*
170 silencing events propagated through dilution of the stable fluorescent protein by cell division. To
171 pinpoint the timing of early regulatory events that give rise to these differences in *Tcf7*-YFP
172 levels, we calculated the *Tcf7* promoter activity over time in single cells, defined as the rate at
173 which total *Tcf7*-YFP levels increase over time, using a Hidden Markov Model (HMM) to assign
174 *Tcf7* promoter activity states to each cell at each timepoint and identify switching points between
175 those states (Fig. 3A-C; Fig. S3A-F; see Methods).
176

177 This analysis revealed that cells silence *Tcf7* expression at variable times after the onset of
178 stimulation, and can do so as early as the first cell division as well as at later generations. Cells
179 activated the *Tcf7* promoter prior to the first cell division, reflecting exit from quiescence, and
180 then proceeded to switch the *Tcf7* promoter to a silent state. The timing at which the *Tcf7*
181 promoter transitioned to the silent state varied between cell tracks both within and between cell
182 lineages, consistent with observed heterogeneity in *Tcf7*-YFP levels within clones (Fig. 3A-D).
183 Removing IL-12 increased the fraction of cells in an active promoter state (Fig. 3C,E). Silent
184 *Tcf7* promoter states persisted across multiple cell divisions (Fig. 3A; Fig. S3I-J) and thus
185 represent heritable regulatory changes as opposed to more transient dynamics such as
186 transcriptional bursting. These results provide evidence that a cell-intrinsic *Tcf7* silencing event,
187 occurring heterogeneously within clones, underlies the early divergence in effector and memory
188 states.
189

190 **A stochastic epigenetic switch controlling *Tcf7* silencing underlies the early effector and**
191 **memory decision**

192 Heterogeneity in *Tcf7* silencing could derive from asymmetric cell division[6,28], whereby cell fate
193 determinants partition unequally, giving rise to discordant behavior between two sister cells.
194 Alternatively, this heterogeneity could result from stochastic control[29–31], whereby two sisters
195 would make *Tcf7* silencing decisions independently. While two sister cells could still make
196 different decisions, they would silence *Tcf7* discordantly no more frequently than expected by
197 chance. To test these predictions, we analyzed the fractions of daughter cell pairs that silence
198 *Tcf7* either discordantly (ON/OFF) or concordantly (OFF/OFF), doing so for cell pairs across all
199 cell generations, with or without IL-12 (Fig. 3F). By plotting concordant (OFF/OFF) versus

200 discordant (ON/OFF) sister pair fractions, we found that all data points adhered to a theoretical
201 curve representing the expected relationship between sister pair fractions for independent
202 regulation (Fig. 3G). Consistently, by statistical analysis using a modified Cohen's kappa
203 coefficient (κ'), we found that daughter cells were no more likely to make discordant decisions
204 than expected by chance (Fig. 3H; Supplementary Table 4). These findings support the view that
205 *Tcf7* silences in a stochastic manner to drive divergent decision making within clones.
206
207 Epigenetic switching mechanisms, involving changes in chromatin modifications or
208 conformation at gene loci, can introduce stochastic rate-limiting steps to gene activation or
209 silencing[32–34]. As *Tcf7* silencing involves repressive DNA or histone methylation[14,20,35,36], it
210 could be gated by such a mechanism. Epigenetic mechanisms act in *cis* at individual gene loci
211 and therefore would silence each *Tcf7* locus independently. To test for this mechanism, we
212 compared *Tcf7*-YFP silencing kinetics in cells from mice homozygous and heterozygous for the
213 reporter, with the prediction that homozygous reporter cells would yield a smaller population of
214 YFP-low cells, since both loci need to silence for loss of reporter expression (Fig. 3I-J, Fig.
215 S3K). Indeed, the *Tcf7*-YFP silent population was significantly smaller in homozygous reporter
216 cells and increased with IL-12, consistent with a *cis*-epigenetic silencing mechanism modulated
217 by inflammation. Together, these results provide evidence that a stochastic *cis*-epigenetic switch,
218 tunable by external stimuli, controls the early decision of naive cells to silence *Tcf7* expression
219 and memory potential.
220
221 **Reversibility of *Tcf7* silencing enables a late memory decision**

222 *Tcf7* silencing has been proposed to be an irreversible event that marks a 'point of no return' for
223 effector differentiation and loss of memory potential[5,37]. Conversely, various studies have
224 demonstrated that cells that acquire cytotoxic effector function are able to populate memory
225 compartments after an infection is resolved[8,9,38], suggesting that *Tcf7*-silenced effectors may still
226 be able to reactivate *Tcf7* and reacquire memory potential. Our data thus far provide evidence for
227 an early T cell decision to abandon or maintain memory potential, driven by stochasticity in
228 antigen-driven *Tcf7* silencing, but do not exclude the possibility that effector cells can reverse
229 their decisions and regain memory potential later after withdrawal of stimulation.
230
231 To test this possibility, we sorted *Tcf7*-YFP low and *Tcf7*-YFP high cells after initial culture and
232 subjected them to reculture with variable stimulation conditions *ex vivo* (Fig. 4A). As expected,
233 sorted *Tcf7*-YFP high cells maintained *Tcf7*-YFP expression without stimulation but underwent
234 heterogeneous silencing under continuing stimulation (Fig. 4B-C, Fig. S4A-B). Furthermore,
235 *Tcf7*-YFP low cells maintained a silent state upon continued stimulation, as observed. Strikingly,
236 however, upon stimulation withdrawal, *Tcf7* reactivated, with the fraction of *Tcf7* expressing
237 cells increasing over 6 days. *Tcf7* reactivation upon stimulation withdrawal coincided with CD25
238 downregulation and CD62L upregulation, suggesting re-entry into a memory state (Fig 4D). To
239 test whether *Tcf7* reactivation and reacquisition of memory potential also occurs *in vivo*, we
240 transferred *Tcf7*-YFP low and high cells into naive recipient mice (Fig. 4A), and assayed their
241 *Tcf7* expression at successive time points. Indeed, *Tcf7*-YFP low cells reactivated *Tcf7*
242 expression progressively in the spleen and lymph nodes over 10 days with concomitant increases
243 in CD62L and IL7Rα, indicating reacquisition of a memory phenotype (Fig. 4E-G; Fig. S4C-D).
244

245 We next used clonal live imaging of sorted *Tcf7*-YFP low cells confined in microwells to test if
246 *Tcf7* reactivation is heterogeneous within individual effector clones, as would be expected if
247 reactivation occurs via reversal of stochastic *cis*-epigenetic silencing (Fig. 3). Consistent with
248 reactivation observed from bulk starting populations, individual *Tcf7* silenced cells gave rise to
249 *Tcf7* high cells (Fig 4H-I; Supplementary Movies 2 and 3; Supplementary Table 5). Similar to
250 the initial *Tcf7* silencing event, reactivation was heterogeneous within clones. Reactivation
251 occurred only after multiple divisions, which may reflect the need for cell division for permissive
252 chromatin state changes. Overall, these results indicate that cells that have silenced *Tcf7* and
253 relinquished memory potential can reverse this decision later, after resolution of an immune
254 challenge.
255
256 ***Tcf7* high cells formed through early and late decisions acquire a common memory**
257 **program**
258 Our results show that memory cells can arise through two pathways: a "naive to memory" (NM)
259 pathway, whereby some cells maintain *Tcf7* expression during initial antigen stimulation, and a
260 "naive to effector to memory" (NEM) pathway, by which cells that have silenced *Tcf7* and
261 entered an effector state can turn expression back on after stimulation removal. To determine
262 whether *Tcf7* high cells emerging through these two pathways both have genomic and functional
263 memory programs, we subjected them to transcriptomic, epigenomic, and cytokine secretion
264 analysis, alongside control *in vivo* naive ($CD44^{-}CD62L^{+}$), memory ($CD44^{+}CD62L^{+}$), and *ex vivo*
265 generated effector cells (Fig. 5).
266

267 Remarkably, NM and NEM cells showed similar memory characteristics, despite different *Tcf7*
268 regulatory history. They were both more similar to naive and memory *in vivo* controls compared
269 to *ex vivo* generated effector cells in their shared expression of memory-defining genes, though
270 they also maintained some effector characteristics, in line with their recent stimulation (Fig. 5A-
271 C; Fig. S5A). Similar to memory controls, NM and NEM cells demonstrated greater TNF-α and
272 IFN-γ secretion upon re-stimulation compared to naive cells (Fig. 5D-E). NM and NEM cells
273 were most similar in global chromatin accessibility to memory controls (Fig. 5F; Fig. S5B-C).
274 NEM cells recovered similar *Tcf7* accessibility to NM cells (Fig. 5G). At the *Ifng* locus,
275 intermediate accessibility of NM and NEM cells between naive and effector controls suggests
276 that both were poised for rapid recall response, and accessibility at other memory- and effector-
277 associated loci support this conclusion (Fig. S5D).
278
279 While NM and NEM cells were largely similar, notable differences in tissue localization and
280 gene expression suggest they may be primed for different functional memory properties *in vivo*.
281 Transferred *Tcf7* high cells showed greater engraftment in secondary lymphoid organs than *Tcf7*
282 low sorted cells, suggesting different homing capabilities (Fig. S5E). NEM cells also had higher
283 expression and accessibility of some effector-associated genes compared to NM, possibly
284 indicative of enhanced effector capabilities or an effector memory state[37,38] (Fig. S5F-G).
285 Overall, both NM and NEM decision strategies give rise to cells with genomic and functional
286 characteristics of memory, suggesting that memory formation may proceed through a flexible
287 decision-making strategy, allowing both for memory and effector divergence during the initial
288 immune challenge and for effector reacquisition of memory potential after the challenge is
289 resolved.

290

291 **Multiple paths to memory enable robust encoding of pathogen experience through memory**

292 **population size**

293 Flexibility in memory decision-making may have functional benefits, and may in particular

294 allow for scaling of memory population sizes with immune response magnitudes. To test this

295 idea, we used mathematical modeling to evaluate different T cell decision-making strategies in

296 their memory outcomes in response to pathogens of different virulence, modeled as having

297 different rates of replication (see Mathematical Appendix). In our first model, we consider the

298 flexible strategy we observed (Fig. 6A). Here, naive T cells (T_n) initially transition to a *Tcf7*-

299 expressing memory-competent state (MC, T_m) that divides upon exposure to pathogen (v), but

300 stops dividing and persists upon pathogen clearance. These cells can either maintain memory

301 competence upon continuing stimulation, or transition to *Tcf7*-silent effector state (T_e), where

302 they control pathogen growth, but are short-lived. Based on our findings (Fig. 3), this transition

303 to an effector state is stochastic, with a probabilistic rate that increases with pathogen. Effector

304 cells can reverse *Tcf7* silencing and re-enter the memory-competent state in the absence of

305 pathogen, as we observe (Fig. 4).

306

307 Mathematical simulations of this flexible decision model recapitulate the canonical features of

308 the T cell response to acute infection (Fig. 6B; Fig. S6A-B). T cells expand rapidly in response to

309 pathogen, reaching a peak 4-8 days after infection onset that consists mostly of effector cells,

310 followed by a contraction to a stable, lower level of memory-competent cells (T_m). Consistent

311 with known studies[1,39], the quantity of memory cells is ~5% of the peak cell number.

312

313 In response to pathogens with varying replication rates, this flexible decision model allows
314 memory cells to form robustly and scale linearly with peak cell expansion numbers. Increasing
315 effector expansion with faster pathogen replication was accompanied by a proportional increase
316 in memory cells, such that the memory fraction relative to the peak T cell number remained
317 constant (Fig. 6B and 6C – top, yellow shading, γ_v>0.02/hr). This relation is given by:

318 $$f_{T_m} = \frac{\beta_{e,m}}{\beta_{e,m}+\delta_e}$$

319 where $\beta_{e,m}$ is the maximum effector to memory conversion rate and $\delta_e$is the effector death rate.
320 This scaling breaks down when pathogen replication is slow (γ_v<0.02/hr): reduced antigen
321 encounter decreases the probability of the early effector cell decision, such that the number of
322 memory cells generated converges to the starting naive cell number rather than increasing with
323 pathogen replication rate. This ensures a baseline level of memory amid weak challenges that do
324 not elicit a full effector response[3].
325
326 To ask whether flexibility is necessary for scalable memory encoding, we analyzed two
327 alternative decision models, where memory decisions are made at only one juncture. The early
328 decision model, where naive cells irreversibly commit to the *Tcf7*-silent effector state, generated
329 robust memory upon challenge with slow-dividing pathogens but cannot reproduce the linear
330 scaling of the memory population to the peak population in response to faster-replicating
331 pathogens (Fig. 6C, middle; Fig. S6C-F; see also Mathematical Appendix). Conversely, the late
332 decision model, where naive cells transition obligatorily to the effector state and decide later
333 whether to regain memory competence, generated constant memory fractions upon stronger
334 challenges but attenuated memory populations in response to weaker challenges (Fig. 6C,

335 bottom; Fig. S6G-H). These analyses underscore the importance of flexibility in memory
336 decision making for optimal long-term immunity against variable threats.
337
338 **Discussion**
339 Our finding that reversible epigenetic silencing of *Tcf7* generates inherent flexibility in the T cell
340 memory decision reconciles two prevailing models for memory development that have often
341 been regarded as mutually opposed. While there is evidence that memory cells can form both
342 directly from naive cells with little or no effector differentiation and from effector cells that
343 dedifferentiate upon infection clearance[8,9], no model has explained how both pathways can
344 coexist. In this mechanism, stochastic control of *Tcf7* silencing enables early divergent memory
345 and effector decision making, and its reversibility enables late effector dedifferentiation. Antigen
346 and inflammatory signals tune the decision-making probabilities at both junctures (Fig. 2-4) and
347 would thereby influence which pathway would predominate across challenges that differ in
348 signal duration and intensity[40]. This study, together with others[33], implicate stochastic epigenetic
349 switches as drivers of cellular diversification in the immune system. Through regulatory events
350 that initiate over timescales spanning cell generations, these switches allow multiple cell
351 populations to emerge in defined numbers without strict spatially-organized cues[41], facilitating
352 division of labor for optimal pathogen defense.
353
354 Our modeling results lay the groundwork for understanding how the adaptive immune system
355 can encode information about the nature and severity of a pathogen in its memory cell population
356 (Fig. 6). In future work, it will be interesting to determine whether other pathogen features, such
357 as antigenicity or latency, may also be encoded quantitatively. Our findings that memory cells

358 emerging from different decision points may differ in their functional properties (Fig. S5E-G)
359 raise the possibility that flexible decision making could underlie qualitative encoding of
360 pathogen information through the generation of heterogeneous memory subsets[37,38]. In future
361 work, it will be interesting to investigate the extent to which each decision pathway is utilized
362 under various threats *in vivo* and whether cells emerging from different pathways are
363 functionally heterogeneous[42].
364
365 Overall, our study highlights the utility of plasticity in cell fate decision making in biological
366 systems. From a strategic standpoint, flexibility enables decision makers to change their minds
367 with new information, allowing them to mount optimal responses amid uncertain
368 circumstances[12]. For immune cells responding to a pathogen, an ability to reassess prior
369 decisions, as opposed to making early commitments, may enable bet-hedging and greater
370 responsiveness as an immune challenge evolves. Observed plasticity in mammalian stem cell
371 fate decision making[43,44] may similarly allow the body to rapidly adapt its regenerative output to
372 changing physiological needs[45]. A fuller consideration of flexibility in cellular decision making,
373 along with its mechanisms and roles, will shed light into design principles of these systems and
374 provide valuable insight for harnessing cells as environmentally-responsive therapeutic agents.
375

Acknowledgments

We thank members of the Kueh, Nourmohammad, and Shendure labs, as well as Philip Greenberg, Jinfang Zhu, and Douglas Fowler for stimulating discussions and feedback, and William Noble for advice on statistical analysis methods. We also thank Sam Nguyen for help with brightfield image cell segmentation. This study was funded by an NIH/NIBIB Trailblazer Award (R21EB027327, to H.Y.K.) an NIH/NHGRI R01 grant (R01HG010632-01, to J.S.), NSF Graduate Research Fellowships (K.A., E.C.C.) , NSF CAREER award (grant No: 2045054, to A.N.), and startup funds from the Bioengineering Department at the University of Washington (H.Y.K.), the Department of Physics at the University of Washington (A.N.), and the Rockefeller University (J.C.). J.S. is an investigator of the Howard Hughes Medical Institute.

Author Contributions

K.A. and H.Y.K. conceived the study and designed the experiments. E.C.C., J.S. and J.C. contributed to experimental design. K.A. and E.C.C. performed the experiments and analyzed the data. J.C. performed the scRNA-seq experiments, and R.D. performed bulk RNAseq and ATACseq. W.Y. performed initial analysis on the scRNA-seq experiments. J.F. and A.L.W performed analysis on imaging data. K.K.H.N. helped set up the *ex vivo* T cell activation system. H.Y.K. developed the mathematical models and O.U., A.N., and H.Y.K. analyzed the mathematical models. A.B. provided the *Tcf7*-YFP reporter mice and guidance. K.A. and H.Y.K wrote the manuscript. E.C.C. contributed to the writing of the manuscript.

Declaration of interests

The authors declare no competing interests.

399

400 **Data availability**

401 The time-resolved single-cell RNA-seq and bulk RNA-seq and ATAC-seq data generated for this
402 study will be deposited in the Gene Expression Omnibus. All other data will be made available
403 upon reasonable request.

404

405 **Code availability**

406 Scripts for processing sequencing and imaging data are written in Python, R, and Matlab and will
407 be made available at https://github.com/KuehLabUW and https://github.com/kathleenabadie.

408 **Figures**

Figure 1

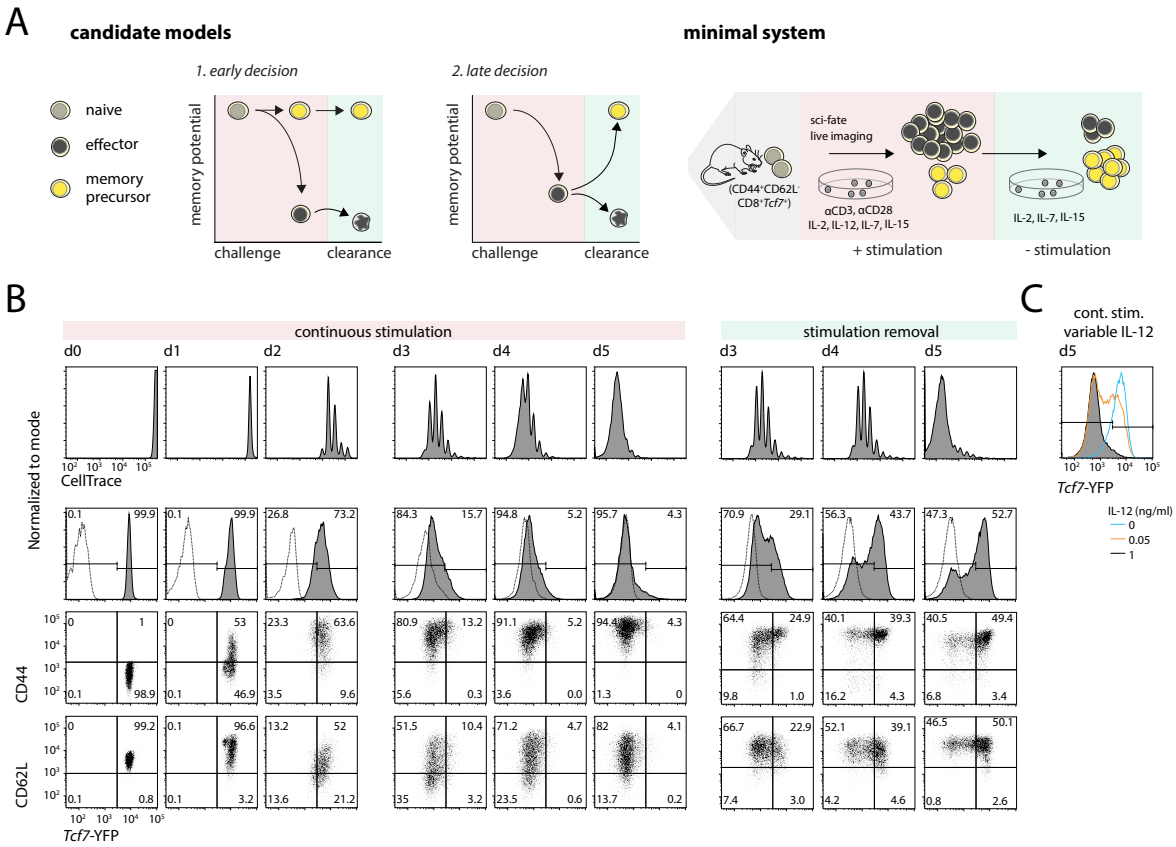

409

410 **Figure 1: A minimal *ex vivo* system to track CD8 T cell effector and memory decision**
411 **making dynamics.** (**A**) Candidate decision-making strategies for CD8 T cell memory generation
412 (left); a minimal *ex vivo* system for tracking memory decision-making dynamics at the single-
413 cell level. (**B-C**) Naive CD8 T cells were isolated from *Tcf7*-YFP reporter mice, then cultured
414 using this minimal *ex vivo* system. Flow cytometry plots show analysis of cultured CD8 T cells
415 during initial stimulation for 2 days (left) and continued stimulation to day 5 (middle), or after
416 stimulation withdrawal (removal of αCD3/αCD28 after day 2 and IL-12 after day 3) (right). (**C**)
417 *Tcf7*-YFP silencing is tunable by IL-12 levels. Data are from a single experiment representative
418 of at least 3 independent experiments.

Figure 2

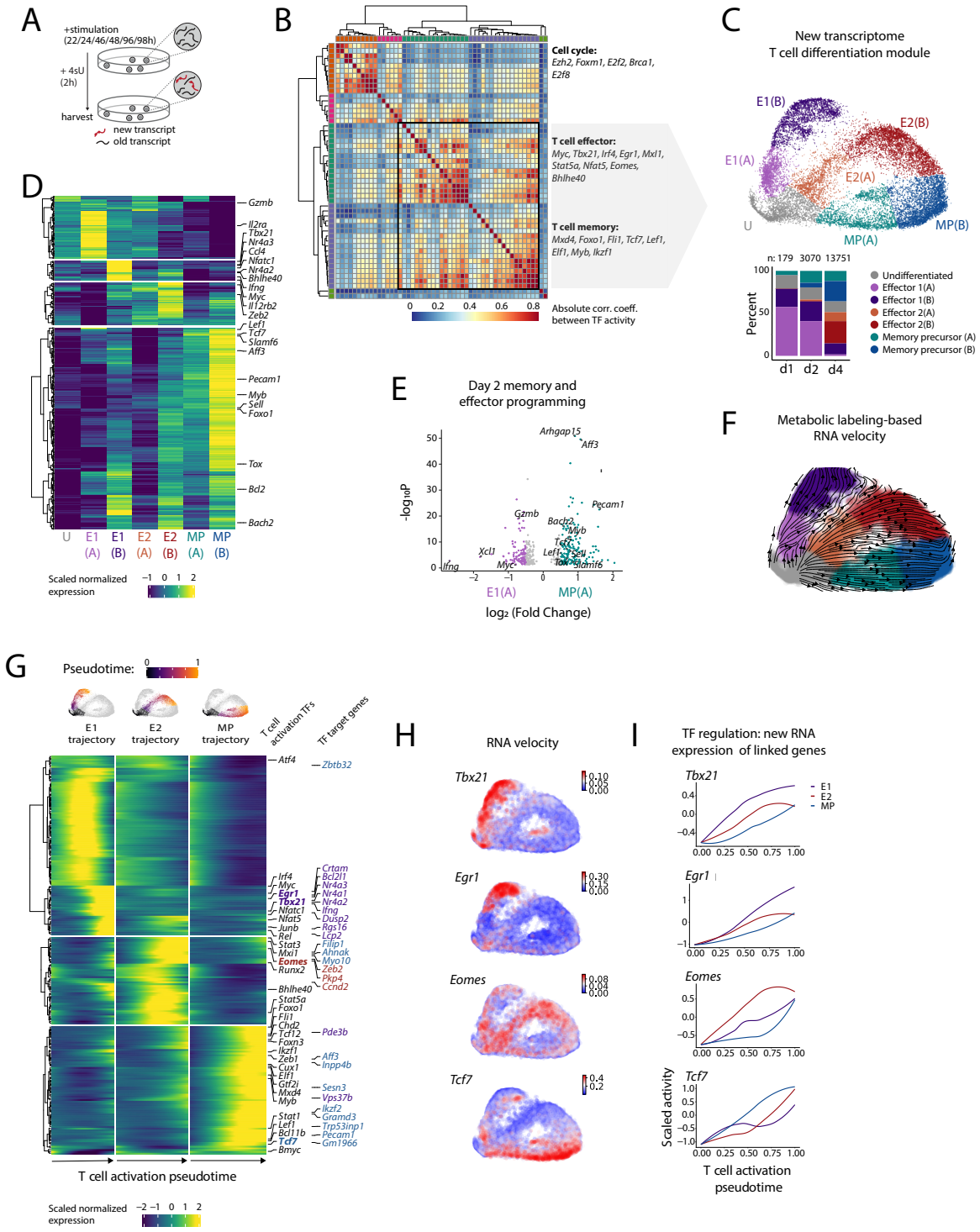
A
+stimulation
(22/24/46/48/96/98h)
+ 4sU
(2h)
harvest
new transcript
old transcript
B
Cell cycle:
Ezh2, Foxm1, E2f2, Brca1, E2f8
T cell effector:
Myc, Tbx21, Irf4, Egr1, Mxl1, Stat5a, Nfat5, Eomes, Bhlhe40
T cell memory:
Mxd4, Foxo1, Fli1, Tcf7, Lef1, Elf1, Myb, Ikzf1
Absolute corr. coeff. between TF activity
C
New transcriptome
T cell differentiation module
E1(B)
E2(B)
E1(A)
E2(A)
U
MP(A)
MP(B)
n: 179 3070 13751
Percent
d1 d2 d4
Undifferentiated
Effector 1(A)
Effector 1(B)
Effector 2(A)
Effector 2(B)
Memory precursor (A)
Memory precursor (B)
D
Gzmb
Il2ra
Tbx21
Nr4a3
Ccl4
Nfatc1
Nr4a2
Bhlhe40
Ifng
Myc
Il12rb2
Zeb2
Lef1
Tcf7
Slamf6
Aff3
Pecam1
Myb
Sell
Foxo1
Tox
Bcl2
Bach2
U E1 (A) E1 (B) E2 (A) E2 (B) MP (A) MP (B)
Scaled normalized expression
E
Day 2 memory and effector programming
Arhgap15
Aff3
Pecam1
Gzmb
Bach2
Myb
Tcf7
Sell
Lef1
Tox
Slamf6
Xcl1
Ifng
Myc
-log10P
E1(A)
MP(A)
log2 (Fold Change)
F
Metabolic labeling-based RNA velocity
G
Pseudotime:
E1 trajectory
E2 trajectory
MP trajectory
T cell activation TFs
TF target genes
Atf4
Zbtb32
Irf4
Myc
Egr1
Tbx21
Nfatc1
Nfat5
Junb
Rel
Stat3
Mxi1
Eomes
Runx2
Crtam
Bcl2l1
Nr4a3
Nr4a1
Nr4a2
Ifng
Dusp2
Rgs16
Lcp2
Filip1
Ahnak
Myo10
Zeb2
Pkp4
Ccnd2
Bhlhe40
Stat5a
Foxo1
Fli1
Chd2
Tcf12
Foxn3
Ikzf1
Zeb1
Cux1
Elf1
Gtf2i
Mxd4
Myb
Pde3b
Aff3
Inpp4b
Sesn3
Vps37b
Ikzf2
Gramd3
Trp53inp1
Pecam1
Gm1966
Stat1
Lef1
Bcl11b
Tcf7
Bmyc
T cell activation pseudotime
Scaled normalized expression
H
RNA velocity
Tbx21
Egr1
Eomes
Tcf7
I
TF regulation: new RNA expression of linked genes
Tbx21
Egr1
Eomes
Tcf7
E1
E2
MP
Scaled activity
T cell activation pseudotime

419

420 **Figure 2: Naive cells diverge into effector and memory states early after activation.** (**A**)
421 Naive CD8 T cells were activated as in Fig. 1A, with 0.05 ng/ml IL-12. After 1, 2, and 4 days,
422 cells were treated with 4sU for 2 hours to label new transcripts, then harvested for time-resolved
423 transcriptomics using *sci-fate*. (**B**) Heatmap showing the absolute Pearson's correlation
424 coefficient between the activities of pairs of TFs, generated using *sci-fate*. Key TFs in each
425 module are labeled at right. T cell differentiation module used for subsequent analysis is boxed.
426 (**C**) UMAP visualization of cells based on the activity of T cell differentiation-related TF
427 module, using newly synthesized mRNA, colored by cluster ID (top). Percentage of cells in each
428 T cell activation state cluster after indicated days (bottom). (**D**) Aggregated expression (scaled,
429 $\log_{10}$ normalized) of top 400 differentially expressed (DE) genes between clusters ($q < 3 \times 10^{-45}$
430 for all genes except for *Ifng*, $q = 7.3 \times 10^{-29}$). (**E**) DE genes between E1(A) and MP(A) at day 2
431 only; log2FC > 0.5 and adj. $p < 0.05$. (**F**) UMAP visualization as in (C), characterized by
432 labeling-based RNA velocity analysis. Streamlines indicate the integration paths that connect
433 local projections from the observed state to the extrapolated future state(*26*). (**G**) Pseudotemporal
434 ordering of top 200 DE genes and additional genes of interest ($q < 1.4 \times 10^{-17}$) between
435 trajectories. Gene labels correspond to all DE TFs in the T cell differentiation TF module (left
436 text) and DE target genes linked to *Tbx21*, *Egr1*, *Eomes*, and *Tcf7* (right text). (**H**) RNA velocity
437 and (**I**) Loess smoothed TF activity over pseudotime for four of the most DE genes between
438 trajectories. TF activity is calculated as the normalized aggregation of levels of newly
439 synthesized mRNA for all TF target genes, scaled across all cells. Cells in the undifferentiated
440 (U) cluster are set to pseudotime = 0 for each trajectory.

Figure 3

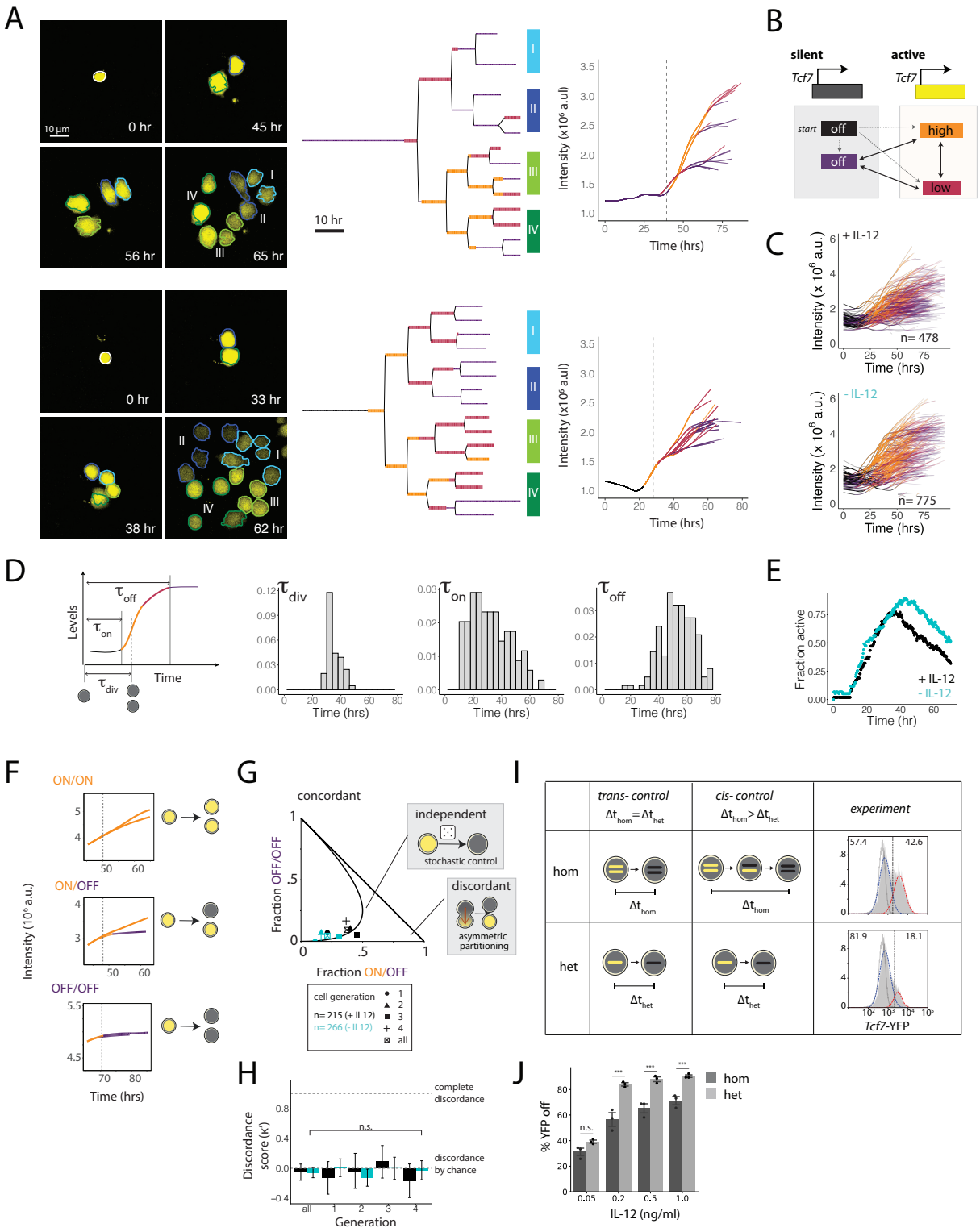
A
10 µm
0 hr
45 hr
56 hr
65 hr
10 hr
Intensity (x10⁶ a.u)
Time (hrs)
0 hr
33 hr
38 hr
62 hr
B
silent
active
Tcf7
start
off
high
low
C
+ IL-12
- IL-12
Intensity (x 10⁶ a.u.)
n= 478
n= 775
Time (hrs)
D
Levels
Time
τoff
τon
τdiv
Time (hrs)
E
Fraction active
+ IL-12
- IL-12
Time (hr)
F
ON/ON
ON/OFF
OFF/OFF
Intensity (10⁶ a.u.)
Time (hrs)
G
concordant
independent
stochastic control
discordant
asymmetric partitioning
Fraction OFF/OFF
Fraction ON/OFF
cell generation
n= 215 (+ IL12)
n= 266 (- IL12)
all
H
complete discordance
discordance by chance
n.s.
Discordance score (K')
Generation
I
trans- control
cis- control
experiment
hom
het
57.4
42.6
81.9
18.1
Tcf7-YFP
J
hom
het
% YFP off
n.s.
IL-12 (ng/ml)

441

442 **Figure 3: Heterogeneous *Tcf7* silencing within clones is controlled by a stochastic epigenetic**
443 **switch.** (**A**) Representative lineages demonstrating clonal heterogeneity in *Tcf7*-YFP silencing:
444 image snap shots (left), lineage trees (middle), and reporter intensity (area x median YFP levels)
445 over time for each track (right), with the first cell division marked by a vertical dashed line. Cell
446 borders in snapshots are colored and labeled to match their corresponding leaves in the lineage
447 trees. Lineage trees and tracks are colored by HMM-derived promoter state, outlined in (**B**).
448 Cells are cultured with 1 ng/ml IL-12 unless otherwise indicated. (**C**) Reporter intensity for all
449 overlaid tracks, colored by promoter state. (**D**) For each track, from left to right: time of first
450 division, time of first transition to a stable active state, time of first transition to a stable silent
451 state (stable state ≥ 10 hrs). (**E**) For all lineages combined, fraction of cells in an active promoter
452 state over time, +/- 1 ng/ml IL-12. (**F-H**) Each division of a parent cell with the *Tcf7* promoter
453 ON was categorized as giving rise to zero, one, or two daughters that transition to an OFF state.
454 (**F**) Examples of each division category. (**G**) The OFF/OFF fraction by ON/OFF fraction is
455 plotted separately for each generation, +/- IL-12, to distinguish concordant, independent, and
456 asymmetric silencing mechanisms. (**H**) Modified Cohen's kappa test for division events in (G).
457 (**I**) Comparison of YFP/YFP and YFP/+ reporters to distinguish *cis* and *trans* regulation of *Tcf7*
458 silencing (left). YFP distributions for YFP/YFP and YFP/+ reporters cultured for 5 days with 0.2
459 ng/ml IL-12 (right). YFP off fractions are calculated from gaussian fits to distributions. (**J**) YFP
460 off percentages as in (I), over a range of IL-12 concentrations. Mean ± s.d. Statistical
461 significance was calculated with an unpaired two-tailed t test; n.s. p=0.05, ***p<0.005.
462 Individual data points are from a single experiment representative of 2 independent experiments
463 (I-J).

Figure 4

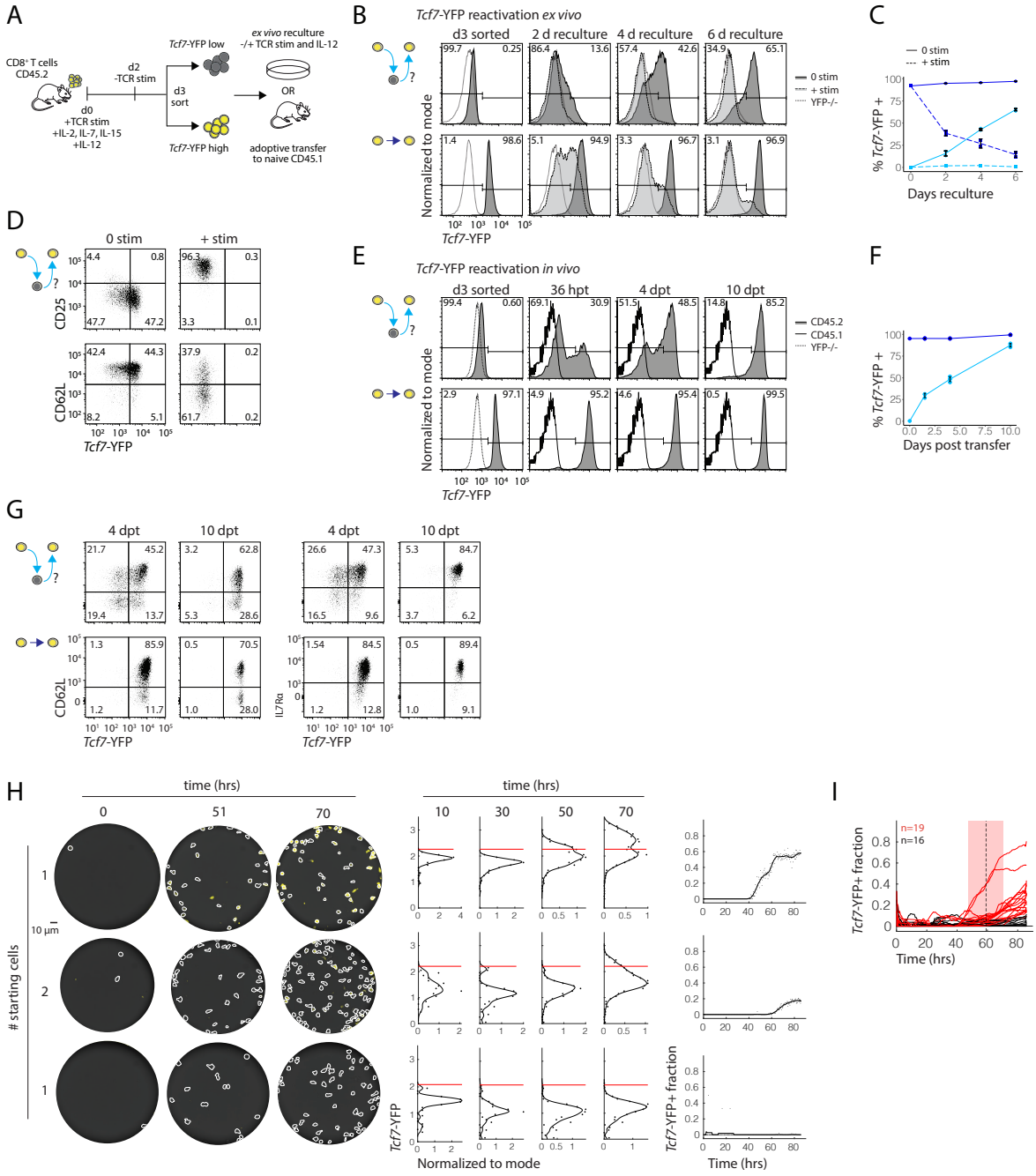
A
CD8+ T cells
CD45.2
d0
+TCR stim
+IL-2, IL-7, IL-15
+IL-12
d2
-TCR stim
d3
sort
Tcf7-YFP low
Tcf7-YFP high
ex vivo reculture
-/+ TCR stim and IL-12
OR
adoptive transfer
to naive CD45.1
B
Tcf7-YFP reactivation ex vivo
d3 sorted
2 d reculture
4 d reculture
6 d reculture
0 stim
+ stim
YFP-/-
Normalized to mode
Tcf7-YFP
C
0 stim
+ stim
% Tcf7-YFP +
Days reculture
D
0 stim
+ stim
CD25
CD62L
Tcf7-YFP
E
Tcf7-YFP reactivation in vivo
d3 sorted
36 hpt
4 dpt
10 dpt
CD45.2
CD45.1
YFP-/-
Normalized to mode
Tcf7-YFP
F
% Tcf7-YFP +
Days post transfer
G
4 dpt
10 dpt
CD62L
IL7Rα
Tcf7-YFP
H
time (hrs)
0
51
70
10 µm
starting cells
time (hrs)
10
30
50
70
Tcf7-YFP
Normalized to mode
Tcf7-YFP+ fraction
Time (hrs)
I
n=19
n=16
Tcf7-YFP+ fraction
Time (hrs)

464

465 **Figure 4: Effector cells reverse *Tcf7* silencing and regain memory potential upon**
466 **stimulation withdrawal.** (**A**) Naive cells from *Tcf7*-YFP mice were stimulated as indicated,
467 sorted for *Tcf7*-YFP low and high populations after 3 days, and recultured either *ex vivo* (B-D,
468 H-I) or adoptively transferred to naive recipients (E-G). Light and dark blue coloring throughout
469 correspond to sorted YFP low and high populations, respectively. (**B-C**) *Tcf7*-YFP levels during
470 reculture with or without αCD3/αCD28 and IL-12 (+/- stim) compared to non-fluorescent
471 controls. **(D)** CD25, CD62L, and *Tcf7*-YFP expression in *Tcf7*-low sorted cells recultured +/-
472 stimulation. (**E-F**) *Tcf7*-YFP levels over time in $CD45.2^{+}CD45.1^{-}CD8^{+}$ cells harvested from the
473 spleen after sort and adoptive transfer to naive recipients. (**G**) CD62L and IL7Rα expression in
474 cells from E, F after *in vivo* transfer. (**H**) Representative microwells of sorted *Tcf7*-low cells
475 recultured without stimulation: snap shots (left), top and bottom wells represent single clones;
476 corresponding histograms (middle) with binned cell data for each time point, with YFP +/- gate
477 drawn at 2 standard deviations above the mean YFP intensity from the first 25 hrs;
478 corresponding YFP^{+} fractions over time (right). (**I**) YFP^{+} fraction for all wells overlaid. Mean
479 activation time = 59.1 hr. [C, F] Mean ± s.d. [B-D] Data are from a single experiment
480 representative of 1 and 3 independent experiments for +stim and 0 stim, respectively. [E-G] Data
481 are from a single experiment with n=3-4 biological replicates.

Figure 5

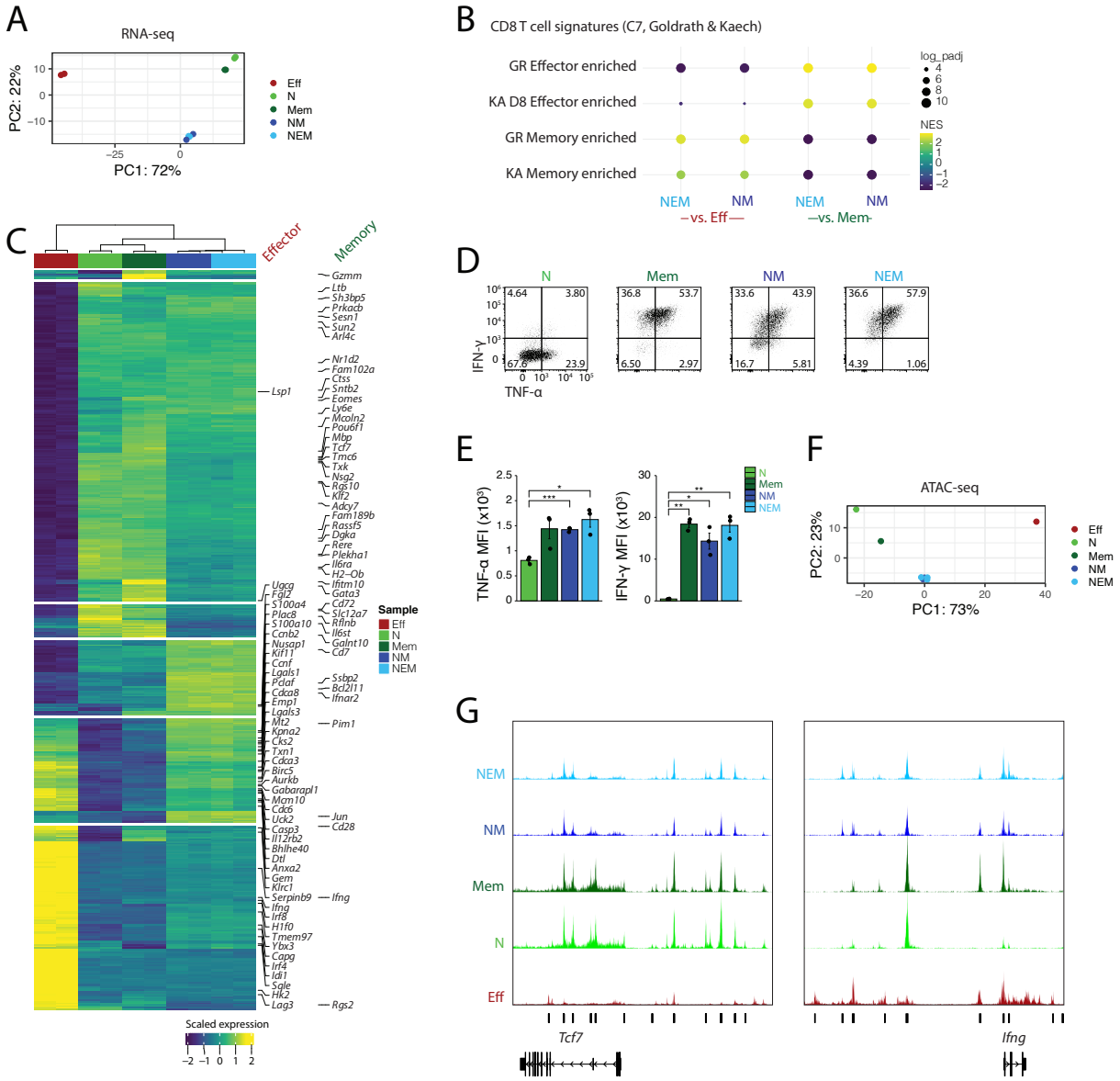

482

483 **Figure 5: *Tcf7* high cells emerging from different routes acquire memory programming**

484 **and functions.** *Tcf7*-YFP low and high cells were sorted after 2 days of stimulation followed by

485 one day of rest, recultured without TCR stimulation or IL-12 for an additional 6 days *ex vivo,*

486 and then sorted for high *Tcf7*-YFP expression and subjected to genomic and functional analyses.

487 (**A**) PCA of RNA-seq profiles (top 500 DE genes) for recultured cells compared to day 3 effector

488 (Eff) and day 0 naive ($CD44^{-}CD62L^{+}$, N) and memory ($CD44^{+}CD62L^{+}$, Mem) controls. NM and

489 NEM cells were sorted as YFP-high and YFP-low on day 3, respectively. (**B**) GSEA of gene
490 signatures from MSigDB (C7, collections deposited by Goldrath (GR) and Kaech (KA)
491 comparing *ex vivo* recultured populations to Eff and Mem controls. (**C**) Heatmap displaying top
492 500 DE genes (lfc ≥ 2, Bonferroni-adjusted p value <0.05) between recultured populations and
493 Eff, N, and Mem controls. Scale bar indicates row z-scores of regularized log transformed count
494 data. Memory and effector associated genes from MSigDB Goldrath and Kaech collections are
495 highlighted. (**D-E**) Cytokine secretion of recultured cells compared to N and Mem controls after
496 PMA/Ionomcyin restimulation. (**F**) PCA of ATAC-seq counts of top 500 differentially accessible
497 peaks between recultured cells and controls. (**G**) ATAC-seq read coverage tracks; vertical bars
498 annotate differentially accessible peaks between recultured cells and controls. [A-C] n = 2
499 biological replicates for each sample. [D-E] Mean ± s.d. Statistical significance was calculated
500 with an unpaired two-tailed t test performed between groups. *p<0.5, **p<0.01, ***p<0.001.
501 Data are n=3 biological replicates from a single experiment. [F-G] n = 1 biological replicate for
502 Eff, N, Mem, n = 2 for NM, n = 3 for NEM.

Figure 6

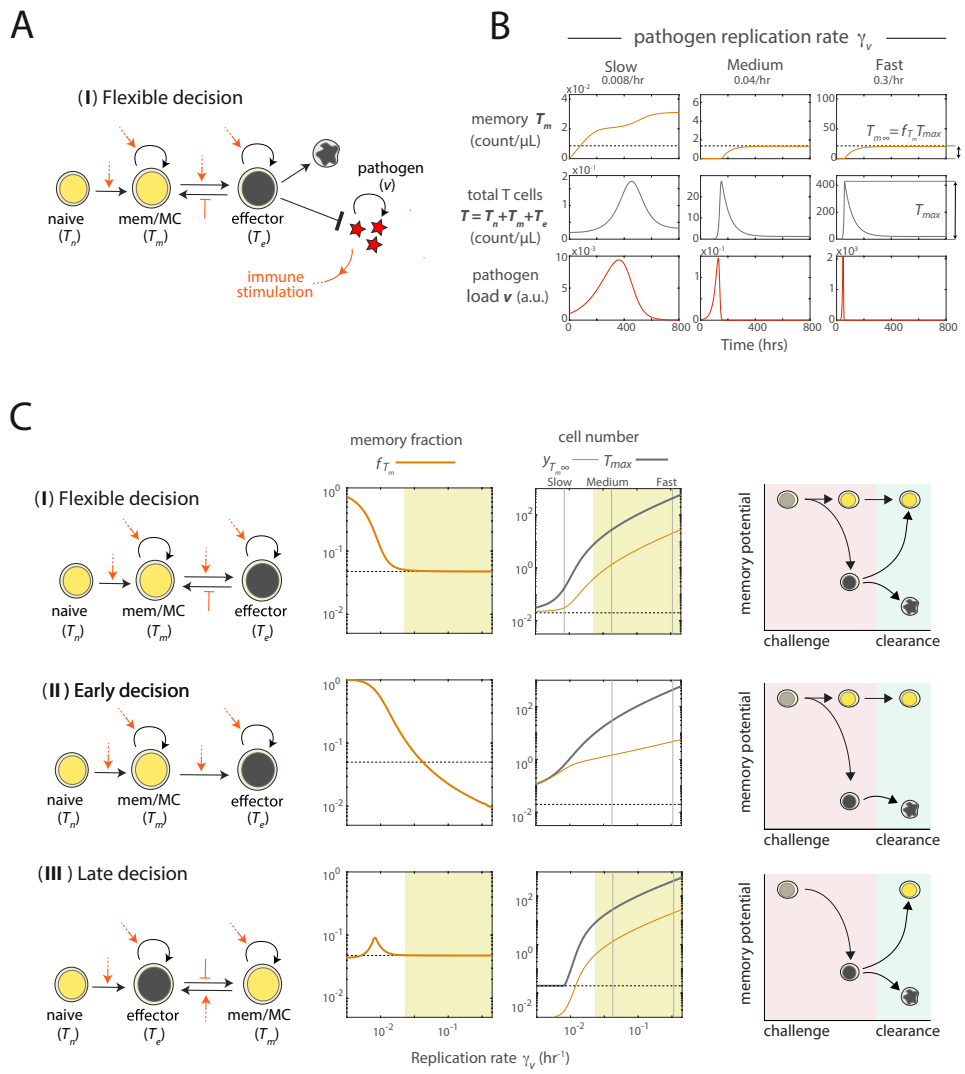

503

504 **Figure 6: Flexible decision making enables quantitative encoding of pathogen experience**

505 **during T cell memory formation.** (**A**) Model incorporates pathogen proliferation, T cell

506 memory decision making through reversible epigenetic switching. Orange arrows indicate

507 modulation of T cell state transitions by pathogen load. (**B**) Time traces show memory T cell

508 levels (top), total T cell levels (middle) and pathogen load (bottom), for different rates of

509 pathogen replication (left to right). Dotted line shows the number of memory T cells formed in

510 the case when this number is a defined fraction of the peak total T cell number, f_{Tm}. (**C**) Distinct

511 strategies for memory decision making: flexible (top), early (middle) or late (bottom); the
512 fraction of T cells at the response peak that become memory cells f_{Tm}; the peak cell number
513 (black) and memory cell number (orange), both plotted against pathogen replication rate γ_v. The
514 dotted line indicates the number of starting naive cells, and the yellow shading marks scalable
515 memory.
516
517 **Methods**
518
519 **Mice**
520 *Tcf7*-YFP mice have been described[16]. We note that a small number of experiments utilized mice
521 harboring an additional non-perturbing *Tbx21*-CFP BAC transgene reporter allele[46], though this
522 reporter was not further analyzed for this study. All mice used in experiments were heterozygous
523 for the *Tcf7*-YFP reporter except where specified. WT C57BL/6 mice (Jackson Laboratory) were
524 utilized as reporter negative controls, where applicable. Both male and female mice were used
525 for *ex vivo* experiments, aged 8 to 12 weeks. Female CD45.1 mice, 8-12 weeks of age, were
526 purchased from the Jackson Laboratory for use as recipients for adoptive transfer experiments.
527 For donors for adoptive transfer experiments, homozygous *Tcf7*-YFP mice were crossed with an
528 LCMV specific TCR transgenic strain[47] (P14) (Jackson Laboratory) and heterozygous offspring
529 were used. P14 homozygous mice without *Tcf7*-YFP were utilized as non-fluorescent controls
530 for sort gate setting. All mice were used in accordance with Institutional Animal Care and Use
531 Committee guidelines for the University of Washington.
532
533 **Naive T cell extraction**

534 Spleens were harvested from mice, massaged between rough glass slides to generate a single-cell
535 suspension, and filtered through 40 µm nylon mesh into HBH (HBSS, 10 mM HEPES, 0.5%
536 BSA, pH 7.4). Cells were spun down for 5 min at 300g, resuspended in 3 ml red blood cell
537 (RBC) lysis buffer (150 mM NH_4Cl, 10 mM $NaHCO_3$, 1 mM EDTA) for 3-5 min, and quenched
538 with HBH. Cells were spun down for 5 min at 300g and resuspended in HBH with 2.4G2
539 blocking solution and incubated for 30 min on ice. Cells were counted, spun down again, and
540 then enriched for CD8 T cells using a $CD8a^+$ T Cell Isolation Kit, mouse (Miltenyi, #130-104-
541 075), with the volume and amount of antibodies and microbeads used scaled down to 70% of
542 that specified by the manufacturer. One LS column was used per spleen (Miltenyi, # 130-042-
543 401). To obtain a pure population of naive CD8 T cells, the cell suspension was stained with
544 anti-CD8 (PerCP/Cyanine5.5, eBioscience, # 45-0081-82 or Biolegend, #100734), anti-CD44
545 (APC or PE, Invitrogen, #17-0441-82, or #12-0331-82), and anti-CD62L (APC/eFluor780,
546 Invitrogen, #47-0621-82) at 1:600 antibody to cell suspension volume ratio in $30x10^6$ cell/ml
547 HBH with Fc block for 15-30 min on ice and then sorted with a BD FACS Aria III (BD
548 Biosciences) with assistance from the University of Washington Pathology Flow Cytometry
549 Core Facility. The naive population was gated as $CD8^+CD44^-CD62L^+$*Tcf7*-YFP^+. Memory cells
550 were gated as $CD8^+CD44^+CD62L^+$*Tcf7*-YFP^+. The cells were sorted into HBH and kept on ice
551 until plating.
552
553 ***Ex vivo* T cell differentiation**
554 One day prior to T cell harvest and activation (day -1), plates were prepared by coating with anti-
555 CD3e (Tonbo, #40-0031-U100), anti-CD28 (Tonbo, #40-0281-U100), RetroNectin (Takara,
556 #T100B), and when specified, anti-CD11a (Biolegend, #101117). Unless otherwise specified,

557 each well of a 96-well plate received 0.2 µg anti-CD3, 0.1 µg anti-CD28, 1 µg Retronectin, and
558 (when specified) 1 µg anti-CD11a in 50 µL of PBS. For differentiation in larger wells, these
559 amounts were scaled up by well surface area. Plates were sealed with parafilm and incubated at
560 4°C overnight. On day 0, plates were allowed to come to room temperature for at least 30 min
561 and washed 2x with PBS. Purified cells were added to wells in T cell media [85% RPMI 1640
562 with L-glutamine, 10% Fetal Bovine Serum, Pen-Strep-Glutamine, 20 mM HEPES, 1 mM
563 Sodium Pyruvate, 0.1 mM NEAA, 50 µM BME] with indicated cytokine concentrations, mixed,
564 and spun down for 1 min at 150g to ensure initial contact for all cells with the coated plate
565 surface. Cytokines added to the media were 100 U/mL IL-2 (PeproTech, # 200-02), 0.5 ng/mL
566 IL-7 (PeproTech, # 200-07), 50 ng/mL IL-15 (PeproTech, # 210-15), and 1 ng/mL IL-12
567 (PeproTech, #210-12) unless otherwise specified. Where specified, IFN-β1 (Biolegend,
568 #581302) was added at 1000 U/mL. The cell seeding concentration was 0.1 - 2.5 million cells /
569 ml unless otherwise indicated. Cells were incubated at 37°C in 5% CO_2 and split every two days
570 by mixing, removing half of the well volume, and topping off the volume with TCM and
571 respective cytokines. Where applicable, prior to seeding, cells were stained with 5 µM CellTrace
572 Violet (CTV) (Invitrogen, #C34557) following the manufacturer's instructions.
573

574 **Flow cytometry analysis**

575 For timecourse analyses with cell surface protein staining, cells were spun down in round-bottom
576 96-well plates or 1.5 ml eppendorf tubes, resuspended in 2.4G2 blocking solution for 15-30 min
577 on ice, stained with cell surface antibodies at 1:1200 (anti-CD8: PerCP-Cyanine5.5, eBioscience,
578 # 45-0081-82, or Biolegend, #100734, anti-CD44: APC, Invitrogen, #17-0441-82, anti-CD62L:
579 APC-e780, Invitrogen #47-0621-82 , anti-CD25: APC, #17-0251-82), 1:400 (anti-CD45.1: APC,

580 Biolegend, #110714), 1:200 (anti-CD45.2: PE/Dazzle594, Biolegend, #109846) or 1:100 (anti-
581 CD127/IL7Rα: PE, Invitrogen, #12-1271-83) antibody to cell suspension volume ratio for an
582 additional 15-30 min on ice, and spun down again for a final resuspension in HBH prior to
583 acquisition. For samples that required intracellular protein staining, cells were fixed and
584 permeabilized using Cytofix/Cytoperm Fixation and Permeabilization kit (BD #554714)
585 according to manufacturer instructions and incubated with antibody for 30 min on ice. The TCF1
586 antibody (PE, BD Biosciences, #564271) and T-bet antibody (PE, Biolegend, #644809) were
587 used at 1:50 and 1:200, respectively. For samples that required intracellular cytokine staining,
588 cells were restimulated for 5 hr with PMA/Ionomycin (1x in 100 µL per sample Thermofisher,
589 #00-4970-93) in round-bottom 96-well plates, with a protein transport inhibitor (1x
590 Thermofisher, #00-4980-93) added after 1 hr. For cytokine secretion after sorting (for Naive,
591 Mem, and NM/NEM) cells were stained with Zombie Near IR at a 1:1000 dilution in PBS
592 following the manufacturer's instructions (Biolegend, #423117). Cells were then fixed,
593 permeabilized, and stained with antibodies for cytokine and other intracellular protein antibodies
594 as described above. All cytokine antibodies were used at 1:100 dilution in 1x BD Perm/Wash
595 buffer (anti-IFN-γ (APC/Cyanine7 or PE, Biolegend, #505849, #505808) and anti-TNF-α
596 (BV711 Biolegend, #506349). Data were acquired using an Attune Nxt Flow Cytometer
597 (ThermoFisher Scientific) and analyzed using FlowJo (BD) software.
598
599 **Sample processing for sci-fate-seq**
600 Naive CD8 T cells were activated *ex vivo*, as described. For this experiment, media was
601 supplemented with 100 U/mL IL-2, 0.5 ng/mL IL-7, 50 ng/mL IL-15, and 0.05 ng/mL IL-12.
602 The moderate level of IL-12, 0.05 ng/ml, was chosen for this experiment to produce a relatively

603 even representation of *Tcf7* high and low cells (see Fig. 1C). At days 1, 2, and 4 of activation,
604 two subsequent sci-fate time points were taken as follows: cells were mixed and split into two
605 wells, which had been coated with anti-CD3 and anti-CD28 at day -1 and remained in the
606 incubator with TCM; 4sU was added to one well for a final concentration of 200 μM, and that
607 well was harvested 2 hr later. At that time, 4sU was similarly added to the second well, and that
608 well was harvested 2 hr later. After each 4sU addition, cells were mixed and spun down at 150g
609 for 1 min. Harvested cells were prepared for sci-RNA-seq as described for the sci-fate protocol
610 [22]. Briefly, cells were fixed with ice-cold 4% PFA for 15 min, washed and flash frozen with
611 PBSR [PBS, pH 7.4, 0.2 mg/ml bovine serum albumin (Fisher), 1% SuperRnaseIn
612 (Thermofisher) and 10 mM dithiothreitol (DTT)]. PFA-fixed cells were thawed, washed, and
613 treated with iodoacetamide (IAA) to attach a carboxyamidomethyl group to 4sU. Following
614 these steps, a single-cell RNA sequencing library was prepared using the sci-RNA-seq
615 protocol[48,49]. The library was sequenced on the Illumina Next-seq system.
616
617 **Computational analysis for sci-fate-seq**
618
619 ***Read alignment, downstream processing, and TF module construction***
620 Read alignment and downstream processing, linking of TFs to regulated genes, and construction
621 of TF modules was performed as described in Cao et al., 2020, with minor modifications.
622 Briefly, for each gene, across all cells, the correlation between mRNA levels of each expressed
623 TF and that gene was computed using LASSO (least absolute shrinkage and selection operator)
624 regression. We sought to comprehensively define gene programs with distinct dynamics by
625 doing this correlation separately both using only newly synthesized transcript levels for potential

626 target genes and using overall transcript levels, expecting that target genes with more stable
627 transcripts would be more readily identified using newly synthesized transcripts, while less
628 abundant, more lowly detected target genes would be more readily identified in the overall
629 transcriptome. After filtering out the resultant covariance links with a correlation coefficient less
630 than 0.03, we identified 2,117 putative TF - target gene covariance links using newly synthesized
631 transcriptome levels and 9,927 using overall transcriptome levels, resulting in a total of 10,405
632 unique links after aggregation. These were further filtered to retain only links supported by ChiP-
633 seq binding, motif enrichment, or predicted enhancer binding[24], resulting in 1065 links between
634 51 TFs and 632 genes. Of these 1065 links, 147 were identified using the newly synthesized
635 transcriptome levels, 649 were identified using the overall transcriptome levels, and 269 were
636 identified by both. To calculate TF activity scores in each cell, newly synthesized unique
637 molecular identifier (UMI) counts for all linked target genes were scaled by library size, log
638 transformed, aggregated, and normalized. The absolute correlation coefficient was computed
639 between all TF pairs with respect to their activity across all cells. Pairwise correlations were
640 hierarchically clustered using the ward D2 method to identify TF modules, with the reasoning
641 that co-regulatory TFs must be simultaneously active within the same cell.
642
643 ***Cell ordering, clustering, and differential gene expression analysis between clusters***
644 We initially attempted to resolve T cell differentiation states by performing dimensionality
645 reduction with Uniform Manifold Approximation and Projection (UMAP) on whole or new
646 transcriptomes using all detected genes. This analysis largely separated cells by the time point at
647 which they were sampled (Fig. S2B), as previously observed[50,51], likely a consequence of the
648 host of other temporal changes occurring during activation apart from differentiation, such as cell

649 cycle control and metabolic programming. To characterize T cell differentiation dynamics apart
650 from other regulatory processes, cells were represented in UMAP space using newly synthesized
651 reads for all genes within the T cell differentiation TF module with monocle3 (v.0.2.3.0)
652 (reduction_method = 'UMAP', umap.n_neighbors = 15L, umap.min_dist = 0.001) [52] using the
653 function align_cds[53] to remove effects of cell cycle phase (preprocess_method = 'PCA',
654 alignment_group = 'Phase'). The resultant UMAP was clustered using density peak clustering[54],
655 which resulted in 5 main clusters (Fig. 2C, U and E2(A) combined, E1(A), E1(B), E2(B), and
656 MP(A) and MP(B) combined). To further resolve observed variable T cell differentiation marker
657 expression within two of these clusters, *k*-means clustering was used to further divide U and
658 E2(A) into separate states and MP(A) and MP(B) into separate states (k = 2 and 2.5,
659 respectively). Cells in different cell cycle phases were relatively evenly distributed across this
660 UMAP, with S phase representation highest in E1(A) (Fig. S2D). Differential gene expression
661 testing was performed between clusters using the monocle3 fit_models function.
662
663 ***RNA velocity analysis***
664 RNA velocity analysis and visualization of velocity streamlines was performed using Dynamo
665 (v.0.95.2.dev)[26] using expression matrices from the full and new transcriptome. The dataset was
666 subsetted to include only the T cell differentiation module genes prior to analysis, but the
667 resultant streamlines were similar when the analysis was performed with all genes. The
668 streamline results were also similar when scVelo (v.0.2.2)[55] was used for velocity analysis (data
669 not shown), with the full and new transcriptome used as the unspliced/spliced expression
670 matrices, indicating that the streamline results are consistent between multiple analysis methods.

671 The scVelo results were also similar with or without subsetting to include only the T cell
672 differentiation module genes.
673
674 ***Trajectory analysis***
675 Cells in each putative trajectory (E1, E2, MP) were ordered in pseudotime based on the point
676 position on the principal curve estimated using the princurve package[56]. To align the precursor
677 cells between trajectories, cells in the undifferentiated (U) cluster were set to pseudotime = 0. To
678 identify genes that distinguish the trajectories, differentially expressed genes were identified
679 using the monocle3 fit_models function with the model formula as the trajectory and pseudotime
680 terms. Only resulting DEG associated with the trajectory term were selected.
681
682 **Time-lapse imaging**
683 Long-term time-lapse imaging of cultured cells, both to track *Tcf7* regulation during initial
684 activation in naive cells and to track *Tcf7* reactivation in sorted *Tcf7*-low cells, was performed as
685 previously described with some modifications[57,58]. Images were acquired with an inverted
686 widefield fluorescence microscope (Leica DMi8) fit with an incubator to maintain a constant
687 humidified environment at 37°C and 5% CO2, using a 40X dry objective. For imaging of the
688 initial 4 days of activation (Fig. 3), cells were seeded at low density (2-5k c/well) in wells of a
689 96-well glass bottom plate (Mattek) coated with anti-CD3, anti-CD28, anti-CD11a, and
690 RetroNectin, as described above. For *Tcf7* reactivation imaging experiments (Fig. 4), *Tcf7*-low
691 cells were sorted on day 3 after 2 days of initial culture with anti-CD3 and anti-CD28 in media
692 with IL-2, IL-7, IL-15, and IL-12 and one additional day of culture with anti-CD3 and anti-CD28
693 removed. These cells were seeded onto PDMS micromesh (250 μm hole diameter,

694 Microsurfaces) mounted on top of a 24-well glass bottom plate (Mattek) to enable clonal
695 tracking, as seeded cells show considerably enhanced motility in the absence of TCR
696 stimulation. To prepare the micromesh for imaging, the surface was first coated with BSA while
697 mounted on top of a 24-well plate overnight at 4°C and then transferred to a new glass well and
698 coated with anti-CD11a and RetroNectin for improved adhesion but without anti-CD3 and anti-
699 CD28. For reactivation experiments, cells were cultured in TCM with IL-2, IL-7, and IL-15, but
700 without IL-12.
701
702 To determine if the experimental conditions required for imaging affect differentiation, we
703 systematically compared expression of CD44, CD62L, and *Tcf7*-YFP in cells activated on glass
704 or tissue culture plates, at high or low seeding density, and with or without presence of anti-
705 CD11a (Fig. S3L). CD44 levels were comparable across all conditions, confirming that all cells
706 activated in all conditions. In tissue culture plates, CD62L and *Tcf7*-YFP levels were also
707 comparable, though the *Tcf7*-YFP levels were slightly reduced at lower cell density, particularly
708 in the condition without IL-12, consistent with previous findings that memory differentiation
709 occurs less efficiently at lower cell densities[59]. On glass plates, the fraction of CD62L low cells
710 was increased compared to on tissue culture plates. *Tcf7* levels were similarly low for the
711 condition with IL-12, but the combination of low seeding density and presence of anti-CD11a on
712 the glass plate resulted in a lower *Tcf7* distribution in the no IL-12 condition than was otherwise
713 observed. This analysis shows that the specific conditions used for imaging do not affect overall
714 differentiation trends but may underestimate the differences in differentiation between conditions
715 with and without IL-12.
716

717 **Computational analysis for time-lapse imaging**

718

719 ***Image segmentation and tracking***

720 Image pre-processing, cell segmentation, and tracking was performed in MATLAB (Mathworks,
721 Natick, MA) using the ictrack movie analysis pipeline we described previously[58,60] (Fig. S3A-B),
722 modified to enable segmentation of cells from brightfield movies. Importantly, to segment cells
723 without additional fluorescent labels besides *Tcf7*-YFP, we first trained a convolutional neural
724 network (CNN) with a U-net architecture[61] to predict fluorescence images of whole cells from
725 brightfield images, using images of cell-trace violet labeled T cells as a training data set[27]. We
726 trained separate CNNs for the images acquired in 96-well plates (Fig. 3) and in microwells (Fig.
727 4), as predictions are optimal when images for training and prediction have similar features. For
728 each training dataset, hundreds of images of CTV-stained cells were acquired at multiple
729 timepoints during the process of interest (e.g. initial T cell activation or culture after stimulation
730 removal). Using the trained CNN, we then generated predicted whole-cell fluorescence images
731 from acquired brightfield movies, which were used for cell segmentation (Fig. S3B, 1.). Briefly,
732 in the ictrack analysis pipeline, images underwent (1) correction by subtraction of uneven
733 background signal stemming from the bottom of the glass plate or the side of the PDMS
734 microwells (2) Gaussian blur followed by pixel value saturation to fix uneven signal intensity
735 within the nucleus of the cell and (3) Laplacian edge detection algorithm to identify the nucleus
736 boundary. Non-cell objects were excluded via size and shape limit exclusions. To generate clonal
737 lineage trees, cells were tracked automatically between adjacent movie frames using the
738 Munkres assignment algorithm, and the resulting cell tracks were manually checked for errors
739 and to annotate cell divisions (Fig. S3B, 2.).

740

741 **Tcf7 *promoter state assignment and analysis***

742 To enable quantitative analysis of *Tcf7* promoter activity in clonal cell lineages, we assembled
743 separate full tracks of total *Tcf7*-YFP fluorescence levels from the starting cell to each ending
744 cell within a lineage tree, for all lineage trees analyzed (Fig. S3B, 3.). Fluorescence levels are
745 halved at each cell division; thus, to ensure continuity in *Tcf7*-YFP levels in these tracks, we
746 calculated for each parent-daughter cell pair an offset in *Tcf7*-YFP levels, that we added to the
747 daughter cells and their progeny, as previously implemented[32]. These 'continuized' tracks were
748 then smoothed using MATLAB medfilt1 (N=5) and smooth (span = 80 time points, equivalent to
749 20 hours, method = lowess), and their first derivatives with respect to time were calculated to
750 generate single-cell tracks of *Tcf7* promoter activity for downstream HMM analysis (Fig. S3B,
751 4.).

752

753 Cell tracks were exported from MATLAB to R for downstream processing. *Tcf7* promoter states
754 for each cell and time point were called from tracks of *Tcf7*-YFP level derivatives using Hidden
755 Markov Model (HMM) modeling, implemented with the msm Package for R (v1.6.9)[62]. We
756 initially tested four candidate HMM models with either three or four promoter states and variable
757 constraints on the derivative ranges within each state (Fig. S3C-D). For each model, we
758 constrained the mean and variance in *Tcf7* promoter activities of each state by fitting Gaussian
759 distributions to the *Tcf7*-YFP derivatives at different time windows, to reflect our observations
760 that cells are expected to be mostly in an inactive, active, or attenuated state at different times.
761 We then compared the performance of these four models by calculating their log-likelihood and
762 corresponding AIC (Akaike information criterion) scores. We also checked the quality of each

763 model's fit to the data by assessing whether residuals of the fit follow a Gaussian distribution[63]
764 (Fig. S3E). Based on this analysis, we chose a model in which cells transition between 4 states:
765 off (initial), low active, high active, and off (Fig. 3B, Fig. S3F), and all start in the off-initial
766 state at the beginning of the track. This four-state model performed favorably compared to other
767 models, likely because it better accounts for the distinct distributions of promoter activity of
768 silent and active cells at initial and later time points.
769
770 Using this four-state model, we assigned promoter activity states at each time point for each cell,
771 removing potentially spurious transient promoter states by finding all promoter states lasting less
772 than 8 hours and replacing them with the previously assigned promoter state. From these states,
773 we then identified promoter silencing events as those involving a switch from active (high or
774 low) to an inactive (off) state, and activation events as those involving a switch from inactive
775 (off-initial or off) to active (high or low) states. We did not allow transitions back to the starting
776 inactive (off-initial) state, as this state has a distinct *Tcf7* promoter activity distribution from the
777 later silent state (off), likely reflecting the distinct noise characteristics of *Tcf7*-YFP levels at
778 different stages after activation.
779
780 For analysis of *Tcf7* silencing between sister cells, we first assigned an ending cell state to all
781 cells in the dataset, representing the final promoter state of the cell prior to division or the end of
782 the cell track. Cells with a tracked duration of less than 3 hours and parents with ending cell state
783 durations of less than 10 hours were also excluded, to ensure the analysis only includes
784 sufficiently tracked cells and durable promoter states. We then collected all division events for
785 which the parent cell was in an ON promoter state prior to division and asked whether the

786 daughter cell tracks ended in an ON or OFF promoter state. We thus calculated the number of
787 division events that lead to no (ON/ON), unequal (ON/OFF), or concordant (OFF/OFF) daughter
788 silencing and then calculated the fractions of each category in the entire dataset and within each
789 generation. To statistically analyze the degree of discordance in *Tcf7* silencing decisions between
790 sister pairs by modifying Cohen's kappa statistical test for inter-rater reliability as follows:
791 division events were categorized as concordant (ON/ON or OFF/OFF) or discordant (ON/OFF)
792 between sisters. The modified Cohen's kappa coefficient, κ', was calculated as the observed
793 percentage of discordant events minus the percentage of discordant events expected by chance,
794 divided by 1 minus the percentage of discordant events expected by chance[64] (Supplementary
795 Table 4).
796
797 **Analysis of *Tcf7*-YFP negative fractions in homozygous and heterozygous reporter cells**
798 For analysis in Fig. 3I-J and Fig. S3K, YFP distributions were exported from FlowJo as csvs,
799 imported to Python, and represented as histograms. The positive and negative populations were
800 fit simultaneously as two gaussian distributions using the scipy.optimize.least_squares function
801 (scipy v1.5.2), and the gate between YFP positive and negative populations was identified as the
802 intersection between the gaussian curves. The silent fraction was then calculated as the sum of
803 the histogram below the gate divided by the sum of the entire histogram. Two-tailed unpaired t
804 tests between homozygous and heterozygous YFP silent fractions were performed using
805 scipy.stats.
806
807 **Sort and adoptive transfer or *ex vivo* reculture of activated cells**

808 Cells were cultured *ex vivo* in the presence of anti-CD3/28 (+TCR stim) and IL-2, IL-7, IL-12,
809 and IL-15 as described. On day 2, cells were transferred to a non-antibody-coated plate (-TCR
810 stim) but kept in the same cytokine environment until day 3 for sorting. For adoptive transfer
811 experiments only, CD8 T cells were activated directly after purifying with the Miltenyi CD8a$^+$ T
812 Cell Isolation Kit using 100% recommended reagent amounts, without further purifying naive
813 starting cells by sorting, and RetroNectin was not used during anti-CD3/anti-CD28 stimulation.
814 Prior to *ex vivo* activation, cells were stained with 2 or 5 μM CellTrace Violet (Invitrogen,
815 #C34557). For *ex vivo* reculture experiments, cells were sorted from a single CellTrace peak
816 representing cells that had undergone the same number of divisions over the 3 day culture period,
817 to ensure YFP differences were due entirely to *Tcf7* regulation differences and not cell division
818 differences. Cells were recultured with and without TCR stimulation and IL-12 (with IL-2, IL-7,
819 and IL-15 maintained except where specified), as labeled in each figure, for an additional 6-10
820 days. For genomics experiments, effector controls (Eff) were activated with TCR stimulation and
821 cytokines for 3 full days. For adoptive transfer, cells were sorted that had undergone at least 4
822 divisions. Cells were sorted on CellTrace Violet and *Tcf7*-YFP levels. The *Tcf7* low gate was set
823 using wild type non-fluorescent control cells that were stimulated identically *ex vivo.* Using this
824 negative gate, the top and bottom 20% of the YFP distribution were selected as *Tcf7* high and
825 low. Sorted cells were resuspended in PBS and transferred retro-orbitally (1 million cells
826 transferred per recipient) to naive CD45.1 mice. On days 1.5, 4, and 10 after adoptive transfer,
827 mice were euthanized, and blood, spleens, and lymph nodes were collected for flow cytometry.
828

829 **Blood and lymph node processing**

830 Blood was collected from euthanized mice by cardiac puncture. Red blood cells were lysed 2x
831 for 5 minutes at room temperature using 1x RBC lysis buffer (described in naive T cell
832 extraction), prior to proceeding with cell staining as described in Flow Cytometry Analysis.
833 Inguinal lymph nodes were harvested, and massaged over a 40 µm cell strainer and resuspended
834 for flow cytometry staining as described in Flow Cytometry Analysis.
835
836 **Sample processing for RNA-seq**
837 Cells were centrifuged at 500g for 5 minutes, resuspended in 350 µL of Trizol (Ambion), mixed
838 well, and frozen at -80°C for processing, starting from step 2 of the RNeasy micro kit (Qiagen,
839 #74004) following the manufacturer's instructions. After processing, RNA was resuspended in
840 RNase free water, quantified using a NanoDrop 2000c (Thermo Scientific), and shipped on dry
841 ice to Novogene Corporation Inc. (Sacramento, CA) for library preparation and sequencing.
842
843 **Computational analysis for RNA-seq**
844 Raw FASTQ files from RNA-seq paired-end sequencing were aligned to the GRCm38/mm10
845 reference genome using Kallisto (v0.46.1)[65], and the resultant transcript-level abundance
846 estimates were imported to genes by cells matrices using tximport (v1.18.0) for downstream
847 analysis. Transcripts with low counts (<10) were removed. Differentially expressed genes were
848 identified with DESeq2 (v1.30.1)[66]. PCA plots were generated using the top 500 differentially
849 expressed genes between NM and NEM samples and naive, memory, and effector controls.
850 Significantly differentially expressed genes were also used for gene set enrichment analysis,
851 performed with fgsea (v1.16.0)[67] and using gene sets from the C7 immunologic or the H
852 Hallmark gene-sets from Molecular Signatures Database deposited by Goldrath and Kaech.

853

854 **Sample processing for ATAC-seq**

855 After sorting, cells were centrifuged at 500g for 5 minutes then supernatant was aspirated
856 without disturbing the pellet. The pellets were resuspended in 100 µL of ATAC freezing buffer[68]
857 (50 mM Tris at pH 8.0, 25% glycerol, 5 mM $Mg(OAc)_2$, 0.1 mM EDTA, 5 mM DTT, 1× protease
858 inhibitor cocktail (Roche-noEDTA tablet), 1:2,500 superasin (Ambion)), flash frozen in liquid
859 nitrogen and stored at -80°C. On the day of processing, samples were thawed, centrifuged at 4°C
860 500g for 5 minutes, and washed with 100 µL of cold 1X PBS. Cells were again centrifuged and
861 resuspended in 100 µL Omni lysis buffer[69] (RSB with 0.1% NP40, 0.1% Tween 20 and 0.01%
862 Digitonin) and incubated on ice for 3 minutes, then quenched with 500 mL of RSB + 0.1%
863 Tween 20. Nuclei were pelleted at 500g for 5 minutes at 4°C, resuspended in 100 µL cold PBS
864 and counted. 50,000 nuclei were used per reaction, pelleted (500g for 5 min at 4°C), resuspended
865 in tagmentation master mix[69] (50 µL total: 25 µL 2X TD buffer, 16.5 µL 1x DPBS, 0.5 µL 1%
866 Digitonin, 0.5 µL 10% Tween 20, 5 µL water, 2.5 µL Tn5 enzyme), and incubated at 55°C for
867 30 minutes. Samples were purified using DNA Clean and Concentrate-5 (Zymo Research) and
868 eluted in EB buffer (10 mM Tris) for amplification of tagmented DNA. PCR amplifications were
869 performed using Illumina indexed primers and NEBNext High-Fidelity 2X PCR Master Mix.
870 SYBR green was added to each PCR reaction to monitor amplification before it reached
871 saturation. Samples in this study were amplified between 11-15 cycles using recommended
872 conditions[70]. Unpurified products were run on a 6% TBE gel for quality control. PCR
873 product/library were purified using DNA Clean and Concentrate-5 (Zymo Research) then ran on
874 a tapestation to visualize nucleosome distribution. The libraries were normalized to 2nM then
875 pooled equimolar for sequencing. Pooled libraries were loaded onto a NextSeq 500 High150

876 cycle kit at 1.5 pM loading concentration with paired ends sequencing (read 1: 74 cycles, read 2:
877 74 cycles, index 1: 10 cycles, index 2: 10 cycles).
878
879 **Computational analysis for ATAC-seq**
880 Raw ATAC-seq FASTQ files from paired-end sequencing were processed and aligned to the
881 mm10 mouse genome using the PEPATAC (v0.10.3)[71] pipeline, which uses bowtie2[72] for
882 alignment. Unmapped, unpaired, and mitochondrial reads were removed. Following alignment,
883 peak calling, merging across all samples, and annotation was performed using HOMER
884 (v4.10)[73]. Differentially accessible regions were identified using DESeq2. PCA plots were
885 generated using the top 500 differentially accessible regions between recultured samples and
886 naive, memory, and effector controls. Coverage tracks were generated from bigwig read
887 alignment files using karyoploteR (v1.14.1).
888
889 **Statistical Analysis**
890 All analyses and p or adjusted p value significance are listed with each figure caption. Statistics
891 were performed in R using the rstatix package (v0.7.0) or Python using scipy (v1.5.2).
892
893

894 **Supplementary tables**

895 **Table S1: Differential gene expression between all UMAP clusters in Fig. 2C.** These DEG
896 results are displayed in heatmap in Fig. 2D.

897 **Table S2: Differential gene expression results for pairwise comparisons between relevant**
898 **UMAP clusters in Fig. 2C.** These DEG results are displayed in volcano plots in Fig. 2E and Fig.
899 S2F.

900 **Table S3: Differential gene expression between E1, E2, and MP trajectories.** These DEG
901 results are displayed in Fig. 2G.

902 **Table S4: Discordance score calculation using modified Cohen's kappa coefficient.** Results
903 are displayed in Fig. 3H.

904 **Table S5: Analysis of *Tcf7*-YFP reactivation in microwells.** The number of microwells with a
905 given starting number of cells and the number of microwells with this number of starting clones
906 that gave rise to *Tcf7*-YFP reactivated cells is shown. Relevant to Fig. 4H-I.

907 **Table S6: Differentially expressed genes in each bulk RNA-seq cluster.** Relevant to Fig. 5C.

908

909 **Supplementary movies**

910 **Movie S1: *Tcf7*-YFP silencing within a clonal lineage.** Relevant to Fig. 3A.

911 **Movie S2: *Tcf7*-YFP reactivation example 1.** Relevant to Fig. 4H-I.

912 **Movie S3: *Tcf7*-YFP reactivation example 2.** Relevant to Fig. 4H-I.

913

914

915

916

917

918

References

1. Murali-Krishna, K., Altman, J.D., Suresh, M., Sourdive, D.J., Zajac, A.J., Miller, J.D., Slansky, J., and Ahmed, R. (1998). Counting antigen-specific CD8 T cells: a reevaluation of bystander activation during viral infection. Immunity *8*, 177–187. 10.1016/s1074-7613(00)80470-7.
2. Vijh, S., and Pamer, E.G. (1997). Immunodominant and subdominant CTL responses to Listeria monocytogenes infection. J. Immunol. *158*, 3366–3371.
3. Busch, D.H., Pilip, I.M., Vijh, S., and Pamer, E.G. (1998). Coordinate Regulation of Complex T Cell Populations Responding to Bacterial Infection. Immunity *8*, 353–362. 10.1016/S1074-7613(00)80540-3.
4. Kaech, S.M., Wherry, E.J., and Ahmed, R. (2002). Effector and memory T-cell differentiation: implications for vaccine development. Nat. Rev. Immunol. *2*, 251–262. 10.1038/nri778.
5. Lin, W.-H.W., Nish, S.A., Yen, B., Chen, Y.-H., Adams, W.C., Kratchmarov, R., Rothman, N.J., Bhandoola, A., Xue, H.-H., and Reiner, S.L. (2016). CD8 + T Lymphocyte Self-Renewal during Effector Cell Determination. Cell Rep. *17*, 1773–1782. 10.1016/j.celrep.2016.10.032.
6. Chang, J.T., Palanivel, V.R., Kinjyo, I., Schambach, F., Intlekofer, A.M., Banerjee, A., Longworth, S.A., Vinup, K.E., Mrass, P., Oliaro, J., et al. (2007). Asymmetric T Lymphocyte Division in the Initiation of Adaptive Immune Responses. Science *315*, 1687–1691. 10.1126/science.1139393.
7. Kakaradov, B., Arsenio, J., Widjaja, C.E., He, Z., Aigner, S., Metz, P.J., Yu, B., Wehrens, E.J., Lopez, J., Kim, S.H., et al. (2017). Early transcriptional and epigenetic regulation of CD8+ T cell differentiation revealed by single-cell RNA sequencing. Nat. Immunol. *18*, 422–432. 10.1038/ni.3688.
8. Youngblood, B., Hale, J.S., Kissick, H.T., Ahn, E., Xu, X., Wieland, A., Araki, K., West, E.E., Ghoneim, H.E., Fan, Y., et al. (2017). Effector CD8 T cells dedifferentiate into long-lived memory cells. Nature *552*, 404–409. 10.1038/nature25144.
9. Bannard, O., Kraman, M., and Fearon, D.T. (2009). Secondary Replicative Function of CD8+ T Cells That Had Developed an Effector Phenotype. Science *323*, 505–509. 10.1126/science.1166831.
10. Jacob, J., and Baltimore, D. (1999). Modelling T-cell memory by genetic marking of memory T cells in vivo. Nature *399*, 593–597. 10.1038/21208.
11. Chung, H.K., McDonald, B., and Kaech, S.M. (2021). The architectural design of CD8+ T cell responses in acute and chronic infection: Parallel structures with divergent fates. J. Exp. Med. *218*, e20201730. 10.1084/jem.20201730.
12. Benjaafar, S., Morin, T.L., and Talavage, J.J. (1995). The strategic value of flexibility in sequential decision making. Eur. J. Oper. Res. *82*, 438–457.
13. Tello-Ramos, M.C., Branch, C.L., Kozlovsky, D.Y., Pitera, A.M., and Pravosudov, V.V. (2019). Spatial memory and cognitive flexibility trade-offs: to be or not to be flexible, that is the question. Anim. Behav. *147*, 129–136.
14. Zhao, X., Shan, Q., and Xue, H.-H. (2021). TCF1 in T cell immunity: a broadened frontier. Nat. Rev. Immunol. 10.1038/s41577-021-00563-6.
15. Jeannet, G., Boudousquie, C., Gardiol, N., Kang, J., Huelsken, J., and Held, W. (2010). Essential role of the Wnt pathway effector Tcf-1 for the establishment of functional CD8 T

964 cell memory. Proc. Natl. Acad. Sci. *107*, 9777–9782. 10.1073/pnas.0914127107.
965 16. Harly, C., Kenney, D., Ren, G., Lai, B., Raabe, T., Yang, Q., Cam, M.C., Xue, H.-H., Zhao,
966 K., and Bhandoola, A. (2019). The transcription factor TCF-1 enforces commitment to the
967 innate lymphoid cell lineage. Nat. Immunol. *20*, 1150–1160. 10.1038/s41590-019-0445-7.
968 17. Mescher, M.F., Curtsinger, J.M., Agarwal, P., Casey, K.A., Gerner, M., Hammerbeck, C.D.,
969 Popescu, F., and Xiao, Z. (2006). Signals required for programming effector and memory
970 development by CD8+ T cells. Immunol. Rev. *211*, 81–92. 10.1111/j.0105-
971 2896.2006.00382.x.
972 18. Rubinstein, M.P., Lind, N.A., Purton, J.F., Filippou, P., Best, J.A., McGhee, P.A., Surh,
973 C.D., and Goldrath, A.W. (2008). IL-7 and IL-15 differentially regulate CD8+ T-cell subsets
974 during contraction of the immune response. Blood *112*, 3704–3712. 10.1182/blood-2008-06-
975 160945.
976 19. Xiao, Z., Casey, K.A., Jameson, S.C., Curtsinger, J.M., and Mescher, M.F. (2009).
977 Programming for CD8 T Cell Memory Development Requires IL-12 or Type I IFN. J.
978 Immunol. *182*, 2786–2794. 10.4049/jimmunol.0803484.
979 20. Danilo, M., Chennupati, V., Silva, J.G., Siegert, S., and Held, W. (2018). Suppression of
980 Tcf1 by Inflammatory Cytokines Facilitates Effector CD8 T Cell Differentiation. Cell Rep.
981 *22*, 2107–2117. 10.1016/j.celrep.2018.01.072.
982 21. Joshi, N.S., Cui, W., Chandele, A., Lee, H.K., Urso, D.R., Hagman, J., Gapin, L., and Kaech,
983 S.M. (2007). Inflammation Directs Memory Precursor and Short-Lived Effector CD8+ T
984 Cell Fates via the Graded Expression of T-bet Transcription Factor. Immunity *27*, 281–295.
985 10.1016/j.immuni.2007.07.010.
986 22. Cao, J., Zhou, W., Steemers, F., Trapnell, C., and Shendure, J. (2020). Sci-fate characterizes
987 the dynamics of gene expression in single cells. Nat. Biotechnol. *38*, 980–988.
988 10.1038/s41587-020-0480-9.
989 23. Erhard, F., Saliba, A.-E., Lusser, A., Toussaint, C., Hennig, T., Prusty, B.K., Kirschenbaum,
990 D., Abadie, K., Miska, E.A., Friedel, C.C., et al. (2022). Time-resolved single-cell RNA-seq
991 using metabolic RNA labelling. Nat. Rev. Methods Primer *2*, 1–18. 10.1038/s43586-022-
992 00157-z.
993 24. He, B., Xing, S., Chen, C., Gao, P., Teng, L., Shan, Q., Gullicksrud, J.A., Martin, M.D., Yu,
994 S., Harty, J.T., et al. (2016). CD8 + T Cells Utilize Highly Dynamic Enhancer Repertoires
995 and Regulatory Circuitry in Response to Infections. Immunity *45*, 1341–1354.
996 10.1016/j.immuni.2016.11.009.
997 25. Best, J.A., Blair, D.A., Knell, J., Yang, E., Mayya, V., Doedens, A., Dustin, M.L., and
998 Goldrath, A.W. (2013). Transcriptional insights into the CD8+ T cell response to infection
999 and memory T cell formation. Nat. Immunol. *14*, 404–412. 10.1038/ni.2536.
1000 26. Qiu, Q., Hu, P., Qiu, X., Govek, K.W., Cámara, P.G., and Wu, H. (2020). Massively parallel
1001 and time-resolved RNA sequencing in single cells with scNT-seq. Nat. Methods.
1002 10.1038/s41592-020-0935-4.
1003 27. Nguyen, P., Chien, S., Dai, J., Jr, R.J.M., Becker, P.S., and Kueh, H.Y. (2021). Unsupervised
1004 discovery of dynamic cell phenotypic states from transmitted light movies. PLOS Comput.
1005 Biol. *17*, e1009626. 10.1371/journal.pcbi.1009626.
1006 28. Verbist, K.C., Guy, C.S., Milasta, S., Liedmann, S., Kamiński, M.M., Wang, R., and Green,
1007 D.R. (2016). Metabolic maintenance of cell asymmetry following division in activated T
1008 lymphocytes. Nature *532*, 389–393. 10.1038/nature17442.
1009 29. Buchholz, V.R., Flossdorf, M., Hensel, I., Kretschmer, L., Weissbrich, B., Graf, P.,

1010 Verschoor, A., Schiemann, M., Hofer, T., and Busch, D.H. (2013). Disparate Individual
1011 Fates Compose Robust CD8+ T Cell Immunity. Science *340*, 630–635.
1012 10.1126/science.1235454.
1013 30. Duffy, K.R., Wellard, C.J., Markham, J.F., Zhou, J.H.S., Holmberg, R., Hawkins, E.D.,
1014 Hasbold, J., Dowling, M.R., and Hodgkin, P.D. (2012). Activation-Induced B Cell Fates Are
1015 Selected by Intracellular Stochastic Competition. Science *335*, 338–341.
1016 10.1126/science.1213230.
1017 31. Gerlach, C., Rohr, J.C., Perie, L., van Rooij, N., van Heijst, J.W.J., Velds, A., Urbanus, J.,
1018 Naik, S.H., Jacobs, H., Beltman, J.B., et al. (2013). Heterogeneous Differentiation Patterns
1019 of Individual CD8+ T Cells. Science *340*, 635–639. 10.1126/science.1235487.
1020 32. Bintu, L., Yong, J., Antebi, Y.E., McCue, K., Kazuki, Y., Uno, N., Oshimura, M., and
1021 Elowitz, M.B. (2016). Dynamics of epigenetic regulation at the single-cell level. Science
1022 *351*, 720–724. 10.1126/science.aab2956.
1023 33. Pease, N.A., Nguyen, P.H.B., Woodworth, M.A., Ng, K.K.H., Irwin, B., Vaughan, J.C., and
1024 Kueh, H.Y. (2021). Tunable, division-independent control of gene activation timing by a
1025 polycomb switch. Cell Rep. *34*, 108888. 10.1016/j.celrep.2021.108888.
1026 34. Lövkvist, C., Mikulski, P., Reeck, S., Hartley, M., Dean, C., and Howard, M. (2021). Hybrid
1027 protein assembly-histone modification mechanism for PRC2-based epigenetic switching and
1028 memory. eLife *10*, e66454. 10.7554/eLife.66454.
1029 35. Gray, S.M., Amezquita, R.A., Guan, T., Kleinstein, S.H., and Kaech, S.M. (2017). Polycomb
1030 Repressive Complex 2-Mediated Chromatin Repression Guides Effector CD8 + T Cell
1031 Terminal Differentiation and Loss of Multipotency. Immunity *46*, 596–608.
1032 10.1016/j.immuni.2017.03.012.
1033 36. Ladle, B.H., Li, K.-P., Phillips, M.J., Pucsek, A.B., Haile, A., Powell, J.D., Jaffee, E.M.,
1034 Hildeman, D.A., and Gamper, C.J. (2016). De novo DNA methylation by DNA
1035 methyltransferase 3a controls early effector $CD8^+$ T-cell fate decisions following activation.
1036 Proc. Natl. Acad. Sci. *113*, 10631–10636. 10.1073/pnas.1524490113.
1037 37. Pais Ferreira, D., Silva, J.G., Wyss, T., Fuertes Marraco, S.A., Scarpellino, L., Charmoy, M.,
1038 Maas, R., Siddiqui, I., Tang, L., Joyce, J.A., et al. (2020). Central memory CD8+ T cells
1039 derive from stem-like Tcf7hi effector cells in the absence of cytotoxic differentiation.
1040 Immunity *53*, 1–16. 10.1016/j.immuni.2020.09.005.
1041 38. Herndler-Brandstetter, D., Ishigame, H., Shinnakasu, R., Plajer, V., Stecher, C., Zhao, J.,
1042 Lietzenmayer, M., Kroehling, L., Takumi, A., Kometani, K., et al. (2018). KLRG1+ Effector
1043 CD8+ T Cells Lose KLRG1, Differentiate into All Memory T Cell Lineages, and Convey
1044 Enhanced Protective Immunity. Immunity *48*, 716–729. 10.1016/j.immuni.2018.03.015.
1045 39. Hou, S., Hyland, L., Ryan, K.W., Portner, A., and Doherty, P.C. (1994). Virus-specific
1046 CD8+ T-cell memory determined by clonal burst size. Nature *369*, 652–654.
1047 10.1038/369652a0.
1048 40. Plumlee, C.R., Sheridan, B.S., Cicek, B.B., and Lefrançois, L. (2013). Environmental Cues
1049 Dictate the Fate of Individual CD8+ T Cells Responding to Infection. Immunity *39*, 347–
1050 356. 10.1016/j.immuni.2013.07.014.
1051 41. Abadie, K., Pease, N.A., Wither, M.J., and Kueh, H.Y. (2019). Order by chance: origins and
1052 benefits of stochasticity in immune cell fate control. Curr. Opin. Syst. Biol. *18*, 95–103.
1053 10.1016/j.coisb.2019.10.013.
1054 42. Wagner, D.E., and Klein, A.M. (2020). Lineage tracing meets single-cell omics:
1055 opportunities and challenges. Nat. Rev. Genet. *21*, 410–427. 10.1038/s41576-020-0223-2.

1056 43. Weinreb, C., and Klein, A.M. (2020). Lineage reconstruction from clonal correlations. Proc.
1057 Natl. Acad. Sci. U. S. A. *117*, 17041–17048. 10.1073/pnas.2000238117.
1058 44. Xin, T., Gonzalez, D., Rompolas, P., and Greco, V. (2018). Flexible fate determination
1059 ensures robust differentiation in the hair follicle. Nat. Cell Biol. *20*, 1361–1369.
1060 10.1038/s41556-018-0232-y.
1061 45. Manz, M.G., and Boettcher, S. (2014). Emergency granulopoiesis. Nat. Rev. Immunol. *14*,
1062 302–314. 10.1038/nri3660.
1063 46. Zhu, J., Jankovic, D., Oler, A.J., Wei, G., Sharma, S., Hu, G., Guo, L., Yagi, R., Yamane, H.,
1064 Punkosdy, G., et al. (2012). The Transcription Factor T-bet Is Induced by Multiple Pathways
1065 and Prevents an Endogenous Th2 Cell Program during Th1 Cell Responses. Immunity *37*,
1066 660–673. 10.1016/j.immuni.2012.09.007.
1067 47. Pircher, H., Bürki, K., Lang, R., Hengartner, H., and Zinkernagel, R.M. (1989). Tolerance
1068 induction in double specific T-cell receptor transgenic mice varies with antigen. Nature *342*,
1069 559–561. 10.1038/342559a0.
1070 48. Cao, J., Packer, J.S., Ramani, V., Cusanovich, D.A., Huynh, C., Daza, R., Qiu, X., Lee, C.,
1071 Furlan, S.N., Steemers, F.J., et al. (2017). Comprehensive single-cell transcriptional profiling
1072 of a multicellular organism. Science *357*, 661–667. 10.1126/science.aam8940.
1073 49. Cao, J., Cusanovich, D.A., Ramani, V., Aghamirzaie, D., Pliner, H.A., Hill, A.J., Daza,
1074 R.M., McFaline-Figueroa, J.L., Packer, J.S., Christiansen, L., et al. (2018). Joint profiling of
1075 chromatin accessibility and gene expression in thousands of single cells. Science *361*, 1380–
1076 1385. 10.1126/science.aau0730.
1077 50. Arsenio, J., Kakaradov, B., Metz, P.J., Kim, S.H., Yeo, G.W., and Chang, J.T. (2014). Early
1078 specification of CD8+ T lymphocyte fates during adaptive immunity revealed by single-cell
1079 gene-expression analyses. Nat. Immunol. *15*, 365–372. 10.1038/ni.2842.
1080 51. Kurd, N.S., He, Z., Louis, T.L., Milner, J.J., Omilusik, K.D., Jin, W., Tsai, M.S., Widjaja,
1081 C.E., Kanbar, J.N., Olvera, J.G., et al. (2020). Early precursors and molecular determinants
1082 of tissue-resident memory $CD8^+$ T lymphocytes revealed by single-cell RNA sequencing.
1083 Sci. Immunol. *5*, eaaz6894. 10.1126/sciimmunol.aaz6894.
1084 52. Cao, J., Spielmann, M., Qiu, X., Huang, X., Ibrahim, D.M., Hill, A.J., Zhang, F., Mundlos,
1085 S., Christiansen, L., Steemers, F.J., et al. (2019). The single-cell transcriptional landscape of
1086 mammalian organogenesis. Nature *566*, 496–502. 10.1038/s41586-019-0969-x.
1087 53. Haghverdi, L., Lun, A.T.L., Morgan, M.D., and Marioni, J.C. (2018). Batch effects in single-
1088 cell RNA-sequencing data are corrected by matching mutual nearest neighbors. Nat.
1089 Biotechnol. *36*, 421–427. 10.1038/nbt.4091.
1090 54. Rodriguez, A., and Laio, A. (2014). Clustering by fast search and find of density peaks.
1091 Science *344*, 1492–1496. 10.1126/science.1242072.
1092 55. La Manno, G., Soldatov, R., Zeisel, A., Braun, E., Hochgerner, H., Petukhov, V.,
1093 Lidschreiber, K., Kastriti, M.E., Lönnerberg, P., Furlan, A., et al. (2018). RNA velocity of
1094 single cells. Nature *560*, 494–498. 10.1038/s41586-018-0414-6.
1095 56. Hastie, T., and Stuetzle, W. (1989). Principal Curves. J. Am. Stat. Assoc. *84*, 502–516.
1096 10.1080/01621459.1989.10478797.
1097 57. Kueh, H.Y., Champhekar, A., Nutt, S.L., Elowitz, M.B., and Rothenberg, E.V. (2013).
1098 Positive Feedback Between PU.1 and the Cell Cycle Controls Myeloid Differentiation.
1099 Science *341*, 670–673. 10.1126/science.1240831.
1100 58. Kueh, H.Y., Yui, M.A., Ng, K.K.H., Pease, S.S., Zhang, J.A., Damle, S.S., Freedman, G.,
1101 Siu, S., Bernstein, I.D., Elowitz, M.B., et al. (2016). Asynchronous combinatorial action of

1102 four regulatory factors activates Bcl11b for T cell commitment. Nat. Immunol. *17*, 956–965.
1103 10.1038/ni.3514.
1104 59. Polonsky, M., Rimer, J., Kern-Perets, A., Zaretsky, I., Miller, S., Bornstein, C., David, E.,
1105 Kopelman, N.M., Stelzer, G., Porat, Z., et al. (2018). Induction of CD4 T cell memory by
1106 local cellular collectivity. Science *360*, eaaj1853. 10.1126/science.aaj1853.
1107 60. Ng, K.K., Yui, M.A., Mehta, A., Siu, S., Irwin, B., Pease, S., Hirose, S., Elowitz, M.B.,
1108 Rothenberg, E.V., and Kueh, H.Y. (2018). A stochastic epigenetic switch controls the
1109 dynamics of T-cell lineage commitment. eLife *7*, e37851. 10.7554/eLife.37851.
1110 61. Ounkomol, C., Seshamani, S., Maleckar, M.M., Collman, F., and Johnson, G.R. (2018).
1111 Label-free prediction of three-dimensional fluorescence images from transmitted-light
1112 microscopy. Nat. Methods *15*, 917–920. 10.1038/s41592-018-0111-2.
1113 62. Jackson, C.H. (2011). Multi-State Models for Panel Data: The **msm** Package for *R*. J. Stat.
1114 Softw. *38*. 10.18637/jss.v038.i08.
1115 63. Lian, H., Thompson, W.A., Thurman, R., Stamatoyannopoulos, J.A., Noble, W.S., and
1116 Lawrence, C.E. (2008). Automated mapping of large-scale chromatin structure in ENCODE.
1117 Bioinformatics *24*, 1911–1916. 10.1093/bioinformatics/btn335.
1118 64. Cohen, J. (1960). A Coefficient of Agreement for Nominal Scales. Educ. Psychol. Meas. *20*,
1119 37–46. 10.1177/001316446002000104.
1120 65. Bray, N.L., Pimentel, H., Melsted, P., and Pachter, L. (2016). Near-optimal probabilistic
1121 RNA-seq quantification. Nat. Biotechnol. *34*, 525–527. 10.1038/nbt.3519.
1122 66. Love, M.I., Huber, W., and Anders, S. (2014). Moderated estimation of fold change and
1123 dispersion for RNA-seq data with DESeq2. Genome Biol. *15*, 550. 10.1186/s13059-014-
1124 0550-8.
1125 67. Korotkevich, G., Sukhov, V., Budin, N., Shpak, B., Artyomov, M.N., and Sergushichev, A.
1126 (2021). Fast gene set enrichment analysis. 060012. 10.1101/060012.
1127 68. Saunders, A., Core, L.J., Sutcliffe, C., Lis, J.T., and Ashe, H.L. (2013). Extensive
1128 polymerase pausing during Drosophila axis patterning enables high-level and pliable
1129 transcription. Genes Dev. *27*, 1146–1158. 10.1101/gad.215459.113.
1130 69. Corces, M.R., Trevino, A.E., Hamilton, E.G., Greenside, P.G., Sinnott-Armstrong, N.A.,
1131 Vesuna, S., Satpathy, A.T., Rubin, A.J., Montine, K.S., Wu, B., et al. (2017). An improved
1132 ATAC-seq protocol reduces background and enables interrogation of frozen tissues. Nat.
1133 Methods *14*, 959–962. 10.1038/nmeth.4396.
1134 70. Cusanovich, D.A., Hill, A.J., Aghamirzaie, D., Daza, R.M., Pliner, H.A., Berletch, J.B.,
1135 Filippova, G.N., Huang, X., Christiansen, L., DeWitt, W.S., et al. (2018). A Single-Cell
1136 Atlas of In Vivo Mammalian Chromatin Accessibility. Cell *174*, 1309-1324.e18.
1137 10.1016/j.cell.2018.06.052.
1138 71. Smith, J.P., Corces, M.R., Xu, J., Reuter, V.P., Chang, H.Y., and Sheffield, N.C. (2021).
1139 PEPATAC: an optimized pipeline for ATAC-seq data analysis with serial alignments. NAR
1140 Genomics Bioinforma. *3*, lqab101. 10.1093/nargab/lqab101.
1141 72. Langmead, B., and Salzberg, S.L. (2012). Fast gapped-read alignment with Bowtie 2. Nat.
1142 Methods *9*, 357–359. 10.1038/nmeth.1923.
1143 73. Heinz, S., Benner, C., Spann, N., Bertolino, E., Lin, Y.C., Laslo, P., Cheng, J.X., Murre, C.,
1144 Singh, H., and Glass, C.K. (2010). Simple Combinations of Lineage-Determining
1145 Transcription Factors Prime cis-Regulatory Elements Required for Macrophage and B Cell
1146 Identities. Mol. Cell *38*, 576–589. 10.1016/j.molcel.2010.05.004.